Translational and Rotational Dynamics
of Supercooled Water

Stephen R. Becker[1]

April 2005

[1]Dept. of Physics, Wesleyan University

Acknowledgments

I would like to thank the Wesleyan students working on the polytheistic linux cluster for their *esprit de corps*. This includes Hongmei Chen, Albert Hill, Scott Knauert, Boris Lukanov, Andrew Rahedi and Dan Slimmon. In particular, I am grateful to Scott for his role in maintaining the linux cluster and to Boris for his friendship and terrible jokes. I am also indebted to my girlfriend, Kim Christensen, and my family, Mary, Charlie and Andy, for encouraging me in all my academic endeavors. Peter Poole was a friendly and enthusiastic collaborator and I owe my data (and a lot more) to him. I am especially grateful for the use of his computers and for being graciously hosted in Nova Scotia in January. And most importantly, I owe thanks to my advisor, Francis Starr, who deserves the most credit for this thesis. He supplied essential technical and physical insight and was a wonderful mentor to have for the past 15 months.

April 2005

TRANSLATIONAL AND ROTATIONAL DYNAMICS OF SUPERCOOLED WATER

STEPHEN R. BECKER

Wesleyan University, Department of Physics 2005

Advisor: Francis W. Starr, Assistant Professor of Physics

ABSTRACT

This thesis presents the results of extensive simulations of the ST2 model of water designed to explore both thermodynamic and dynamic properties in supercooled states. Constant volume simulations were performed at 1,233 state points, with densities ranging from 0.80 g/cm^3 to 1.20 g/cm^3 in steps of .01 g/cm^3; along these isochores, simulations were run at temperatures from 250 K to 400 K in 5 K intervals. Our results qualitatively reproduce many of the expected properties of supercooled water such as the density anomaly and a novel low-temperature phase transition between two liquid states. The Stokes-Einstein and Debye-Stokes-Einstein equations provide a simple hydrodynamic relation between viscosity and diffusion. These relations hold for simple liquids, but are known to fail near a glass transition. For ST2 water, we find that the Debye-Stokes-Einstein equation does not hold at low temperatures. Furthermore, the data indicate that rotational diffusion is enhanced at low temperatures relative to translational diffusion. We also uncover an unexpected connection between dynamics and thermodynamics; specifically, we find that the structural relaxation time τ_α along the critical isochore provides a precursor to the liquid-liquid phase transition at temperatures up to 150 K above the critical temperature. We observe a nearly identical signature in τ_α at a higher density which may indicate a second liquid-liquid phase transition, adding credibility to the recent idea that there may be more than one liquid-liquid critical point.

Contents

List of Figures

Chapter 1

Introduction

1.1 Stable, Metastable and Glassy Water

1.1.1 Water in Nature: Motivation for Study

Water is abundant in the natural world and is the most important chemical for human life. While it is mostly found in stable forms on Earth - the only chemical compound that naturally occurs in all three phases - water can also appear in metastable forms such as supercooled water or glassy water. Supercooled and glassy water have liquid-like structures, which is why they are essential to many biological processes. Crystallization of liquid water into ice nearly always kills biological cells, and therefore living creatures that live in subfreezing temperatures need some mechanism to prevent the crystallization of their internal water-based fluids. Many organisms introduce chemicals or proteins as a sort of anti-freeze into their blood in order to prevent the onset of heterogeneous nucleation, and thus live with "supercooled blood." For example, coldwater fish live with their blood permanently at $-1.5°$C, a full degree below the freezing point of blood [1]. Freezing poses a problem for plants as well. Cryo-preservation techniques in the laboratory require cold temperatures without crystallization. Glasses are responsible for the suspension of desert insect life during drought [2].

Supercooled water is important in non-biological processes as well. Pharma-

ceutical companies may be concerned with whether amorphous drugs will crystallize over time, and food companies may be similarly concerned about food products. Supercooled water is also important in preventing hydrate formation in natural gas pipelines [3]. Clouds are the largest reservoir of supercooled water naturally occurring on Earth. The form of water in clouds is important for climate models, as the radiative and reflective properties of water depend on its phase [1]. Supercooled water and glassy water may also occur on extraterrestrial objects; it is believed that most of the water in the universe is glassy water that makes up comets.

An understanding of supercooled and glassy water would help with understanding the glass transition in general. Glasses are ubiquitous in nature, and found as well in the processing of foods, the commercial stabilization of labile biochemicals, ordinary window glass, optical fibers, plastics, some kinds of silicon photovoltaic cells and even in metals [4, 5]. On the Earth, glass is formed naturally by volcanic events, including the well-known glass obsidian [2]. The transition between glasses and supercooled liquids is not completely well-understood yet, and studying supercooled water gradually adds to our knowledge of the supercooled and glassy phases of all materials. See references [3] for a brief survey of supercooled and glassy water, and [4, 2] for surveys on glass in general.

Furthermore, it was suggested in 1992 [6] that water has a liquid-liquid transition and in 2003 [7] that it has several liquid-liquid transitions. It is not yet known which substances have liquid-liquid transitions, or even if all substances have them. It is suggested since 1963 that carbon has such a transition [8, 9, 10, 11, 12, 13], and recently there has been evidence for such transitions in silicon, phosphorus and SiO_2, which have similar tetrahedral geometry to water [14], as well as for Ge and GeO_2 [15]. However, it does not appear that tetrahedral geometry is necessary for such transitions [14], and atomic liquids such as Se, Te, Rb and Cs have been suggested as potentially having liquid-liquid transitions [15]. Studying the liquid-liquid transition in water will hopefully elucidate the nature of liquid-liquid transitions in general.

1.1.2 Water at 1 Atm.

A molecule of water is comprised of one oxygen atom and two hydrogen atoms. The hydrogen atoms bond to the strongly electronegative oxygen atoms and therefore have a slightly positive charge. The intramolecular OH bond distance is 0.957 Å and is approximately 1/3 ionic and 2/3 covalent in character [16]. The HOH angle is 104.5°, close to the tetrahedral angle of $\approx$ 109.5°. As a result, water tends to form hydrogen bonds with other atoms. In bulk water, the hydrogen atoms form strong (compared to the London dispersion force) inter-molecular hydrogen bonds with oxygen atoms from other molecules; each oxygen atom hydrogen bonds with two hydrogen atoms from other molecules. Because of this, water forms tetrahedral networks, either in a crystal lattice, as in ordinary ice, or in a distorted form without long-range order, as in the liquid. These tetrahedral networks are open, meaning they are less dense than random configurations, but are organized and therefore have less entropy. At low temperatures, energy and entropy are therefore negatively correlated with volume, in contrast to typical liquids [16].

Water, like most substances, has three standard phases: crystal, liquid and gas. The behavior of water at atmospheric pressure (1 Atm.) is shown in Figure 1.1. The melting and boiling temperatures of water depend on the pressure and are shown in Figure 1.5. There are polyamorphic forms of the crystal, meaning that there are more than one stable crystalline structures. In fact, water has over a dozen crystal forms, including nine stable states (ices II, III, V, VI, VII, VIII, X, XI and ordinary hexagonal ice I_h) and four metastable states (ices IV, IX, XII and cubic ice, I_c) [16]. Slow cooling of water at atmospheric pressure results in I_h.

Water can be heated above the boiling temperature without boiling or cooled below the freezing temperature without freezing, and water in these states is referred to as superheated or supercooled, respectively. Superheated and supercooled water are known as "metastable," meaning that they are not in the lowest free energy state. In the case of supercooled water, the lowest free energy state is always a crystal lattice. The discrepancy in energy between the crystalline
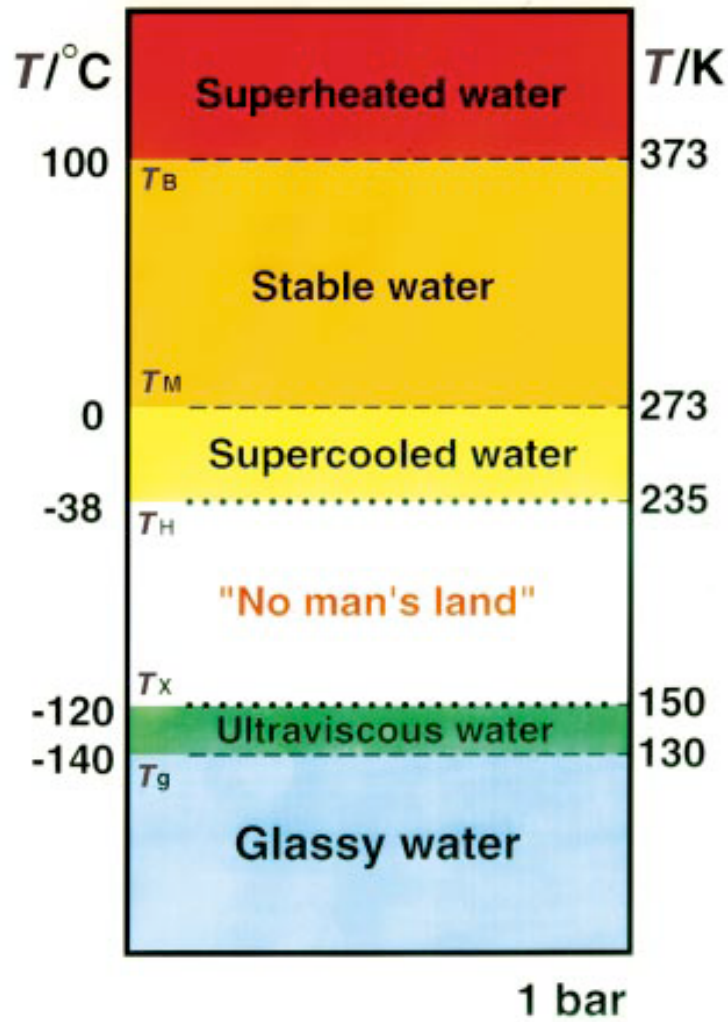
Figure 1.1: Water at 1 Atm.

The Phase Diagram of Water at 1 Atm., from [17].T_B is the boiling temperature, T_M is the melting temperature, T_H is the homogeneous nucleation temperature, T_X is the temperature where glasses crystallize upon heating, and T_g is the glass transition temperature. 1 Atm. =m 760 torr = 1.013 bar = 0.1013 MPa.

and liquid state increases as the temperature is lowered; hence, the typical time needed for crystallization, τ_x, decreases as the temperature is lowered. Thus there are practical limits as to how much the liquid can be cooled. At atmospheric pressure, water can be superheated up to about 280°C and supercooled down to about −42°C [1].

As in all liquids, the onset of crystallization can be shifted to lower temperatures by reducing the number of nucleation-inducing impurities [16]. This is achieved by both purifying the sample and reducing the size. Water is cooled to −42°C by reducing impurities to 10^{12} l^{-1} and using droplets 5 μm in diameter. On average, such a drop will contain only one impurity, but even so the droplet will remain liquid for only 10^{-5} s [16]. Such conditions actually exist in cirrus clouds, and liquid water has been observed as low as -40°C in these clouds [1]. When water crystallizes due to impurities, the process is called heterogeneous nucleation. At low enough temperature, τ_x is so short that it does not remain liquid long enough to be studied. At this point, water is said to have homogeneously nucleated, and there is an experimentally defined pressure-dependent homogeneous nucleation temperature T_H. In this regime, any random occurrence of a tetrahedral shape among only a small cluster of molecules is enough to seed a whole lattice.

At cold enough temperatures, the structural relaxation time τ_α becomes much longer than τ_x due to the inherent sluggishness of the molecules at low temperatures. Thus, if water is cooled quickly enough - faster than τ_x - and to a low enough temperature (below the glass transition temperature T_g), it becomes a vitreous liquid known as a glass. Most liquids will form into a glass; some liquids vitrify easily (i.e. they can be cooled slowly and still form a glass, like SiO_2) while others do not. Glasses can also be made by compressing crystals. A glass is structurally similar to a liquid but because it is colder, it relaxes so slowly that it behaves like a solid on experimental time scales. Glasses will expand to take on the shape of their containers just like liquids, only it may take 10^5 years to do so, as in the case of ordinary window glass. It is hard to create a well-defined criterion for distinguishing between a liquid and a glass, but a practical definition is to call the material a glass when the viscosity is greater than 10^{13} poise [2].

A nearly equivalent definition is that a material is a glass when the structural relaxation time T_α is 100 seconds or greater. The glass transition temperature defined by these criteria is a kinetic event and not a fundamental thermodynamic event. The glass transition temperature for water at atmospheric pressure has long been believed to be around 136 K [18, 19], though recent work has argued that it is 165 K [20, 21].

Upon heating, glasses gain enough mobility to sample more configurations and will therefore lower their energy by crystallizing. For glassy water, this pressure-dependent temperature is referred to as T_x and is around 150 K at atmospheric pressure [16]. Hence there is a "no-man's-land" between T_x and T_g where liquid water can exist but only ephemerally and therefore no experiments have been done in this regime.

In the past two decades, computational and experimental evidence has shown that water has two distinct phases in the liquid and glass regime, known as either high-density liquid (HDL) and low-density liquid (LDL) or high-density amorphous ice (HDA) and low-density amorphous ice (LDA), depending on the temperature [16, 22]. As a result, there is a second critical point, C' (located below 0 K, since no such phase transition is observed in ordinary conditions) [6]. There is much unknown about supercooled and glassy water because it is hard to experiment with and time-consuming to simulate. It is the purpose of this thesis to simulate supercooled water and explore various dynamical quantities, which we will define later.

1.2 Thermodynamics

1.2.1 Typical Liquids

Common thermodynamic state variables include pressure, P, temperature, T, number of particles, N, volume, V, energy, U, and entropy, S. The density is defined $\rho = N/V$. The terms "isochore", "isobar", and "isotherm" refer to conditions of constant density, pressure, or temperature, respectively. The quantity

G, called the Gibbs free energy, is defined $G \equiv U - TS + PV$. A consequence of thermodynamic laws is that substances "seek" to minimize G given a particular T and P. V, N, G, U, and S are extensive variables, meaning that, for example, if two identical systems are combined, the new system has twice the volume, twice the number of particles and twice the free energy. Such a system would not have twice the prior temperature nor twice the prior pressure, and thus T and P are known as intensive variables.

The following relations concerning G hold:

$$\left(\frac{dG}{dT}\right)_{N,V} = -S, \quad \left(\frac{dG}{dP}\right)_{N,T} = -V, \quad \left(\frac{dG}{dN}\right)_{P,T} = -\mu, \tag{1.1}$$

where μ is the chemical potential. Phase transitions (e.g. liquid to crystal) involve discontinuities in S, V and μ, and are conventionally referred to as 1st order transitions because S, V and μ are first derivatives of G. These variables can in turn be used to define response functions such as isothermal compressibility, K_T, specific heat at constant pressure, C_P, and the thermal expansion coefficient, α_P. These variables are defined as

$$K_T = -\frac{1}{V}\left(\frac{dV}{dP}\right)_T, \quad C_P = T\left(\frac{dS}{dT}\right)_P, \quad \alpha_P = \frac{1}{V}\left(\frac{dV}{dT}\right)_P, \tag{1.2}$$

and are thus defined in terms of the second derivative of G. Transitions involving discontinuities in these variables are known as second-order transitions. A major concern with interpreting data is whether thermodynamic variables change continuously or discontinuously. Due to experimental limitations, this is not always straightforward.

The familiar ideal gas law, $PV = NkT$, where k is Boltzmann's factor, is an example of an equation of state. An improved equation of state, know as the Van der Waals equation of state, predicts phase changes as show in Figure 1.2. The Van der Waals equation is

$$\left(P + \frac{N^2 a}{V^2}\right)(V - Nb) = NkT \tag{1.3}$$

or equivalently,

$$\left(P^* + \frac{3}{(V^*)^2}\right)\left(V^* - \frac{1}{3}\right) = \frac{8}{3}T^* \tag{1.4}$$

where b is the volume of each particle, a is a mean-field attraction between particles, and $P^* = P/P_c$, $V^* = V/V_c$ and $T^* = T/T_c$ are unitless pressure, volume and temperature, respectively, as seen in Figure 1.2. The Van der Waals equation provides a qualitative description of many liquids, though it fails in cases of liquids like water.

In Figure 1.2, there is no distinction between phases when $T^* > 1$. Any gas with attractive interactions will have such critical points between the gas and liquid phases. At lower temperatures, the substance can no longer follow the equation of state trajectory because it involves the unphysical unstable region where K_T becomes negative, meaning that volume increases with pressure. When $V^* < 1$, the substance is a liquid, and when $V^* > 1$ it is a gas. Upon expansion, the substance "skips" abruptly at constant pressure (hence with a discontinuity in volume) to the other side of the unstable area. Note that if the volume were to be fixed inside this unstable region, one observes the coexistence of the stable gas and liquid. Liquids "prefer" to change states at the coexistence line because this would lower their Gibbs free energy, but there is no kinetic requirement that they do so, and they can continue to exist in the metastable regime until K_T becomes negative (the statepoints where this happens form the "spinodal" line). Such spinodal lines exist only for the liquid-gas transition; however, it has been suggested that the liquid-gas spinodal line "reappears" below T_g which would explain the existence of HDA and LDA [23]; this theory is known as the stability limit conjecture. There are actually other explanations for abrupt density change between HDA and LDA [16], including the singularity-free scenario [24, 25, 26]. However, experimental evidence suggests that the second critical point scenario is the most likely explanation [27, 28, 29].

Figure 1.3 shows a pressure-temperature diagram for a generic substance. T_C, P_C and ρ_C denote the temperature, pressure and density at the critical point, respectively. At temperatures and pressure above T_C and P_C, there is no distinction betwen a liquid and a gas. In this range, increasing the pressure along an

isotherm, as in Figure 1.2, will result in only continuous changes in volume. More on thermodynamics can be found in a multitude of thermodynamic textbooks and also in statistical mechanics books such as refs [30, 31].
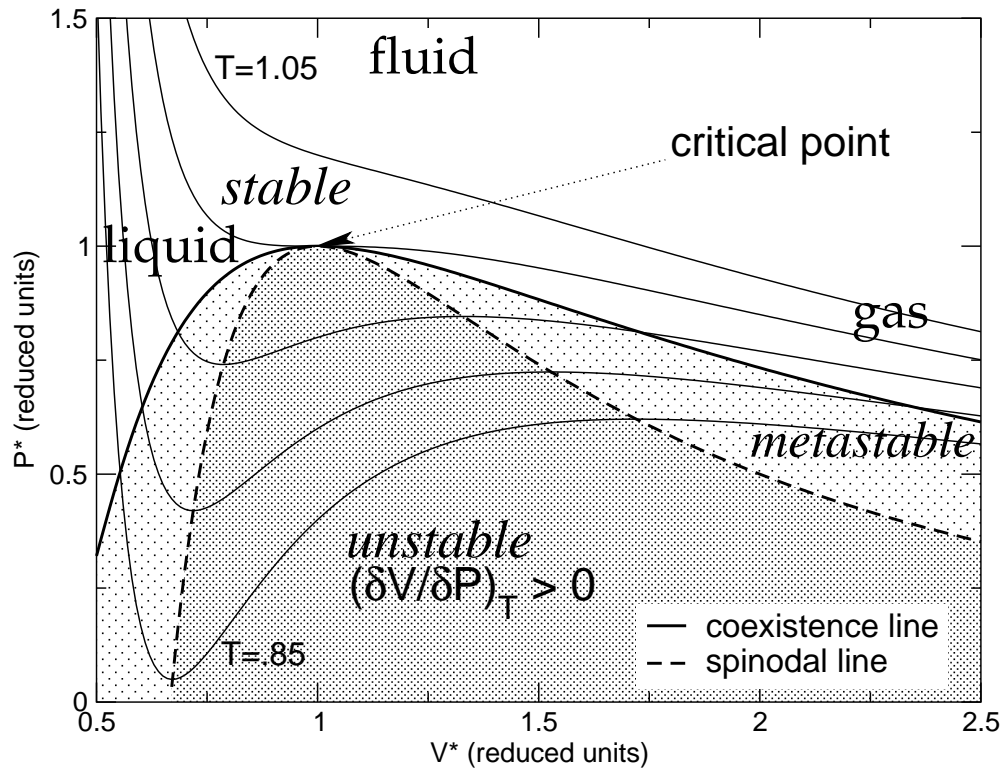
Figure 1.2: PV Diagram for Van der Waals equation of state

Isotherms of the Van der Waals equation of state. Substances with pressures and volumes within the lightly shaded regions are metastable (i.e. supercooled or superheated) while substances in the darkly shaded region are unstable. In the unstable region, substances expand when pressure is increased, which is unphysical. All units are in reduced units, where $P^* = P/P_c$, $V^* = V/V_c$ and $T^* = T/T_c$.
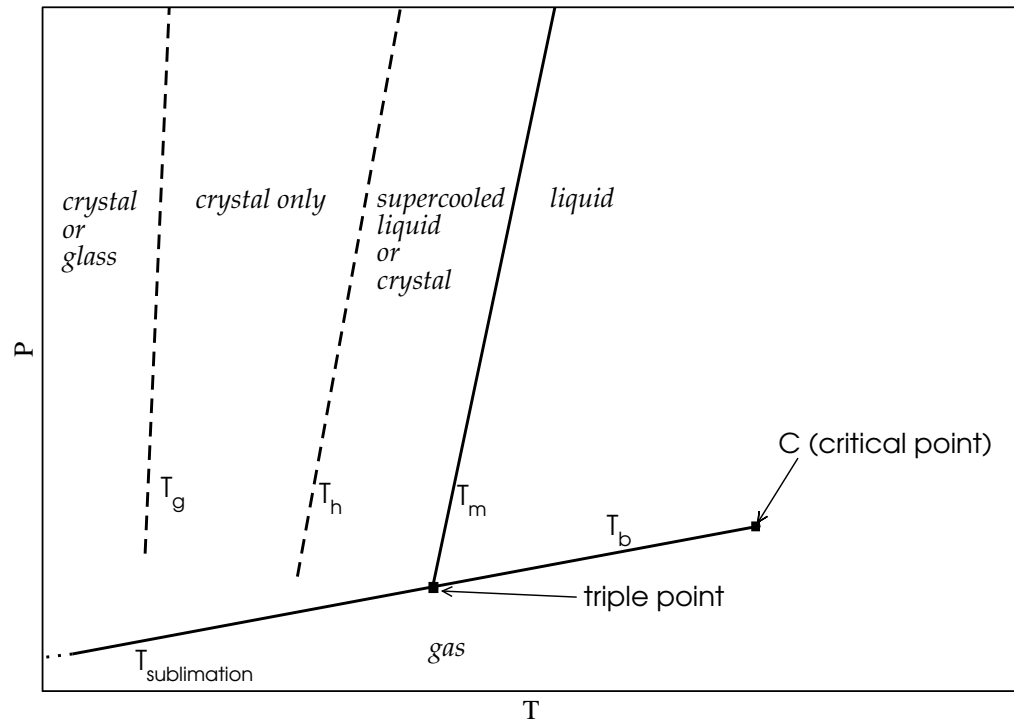
Figure 1.3: Generic PT Diagram

Show above are qualitative features of a generic PT diagram for a substance. Not all substances have a homogeneous nucleation temperature (T_h), meaning that a supercooled liquid can exist until it kinetically changes into a glass. T_b is the boiling temperature, T_m is the melting temperature, $T_{sublimation}$ is the sublimation temperature and T_g is the glass transition temperature.

1.2.2   The Case of Water
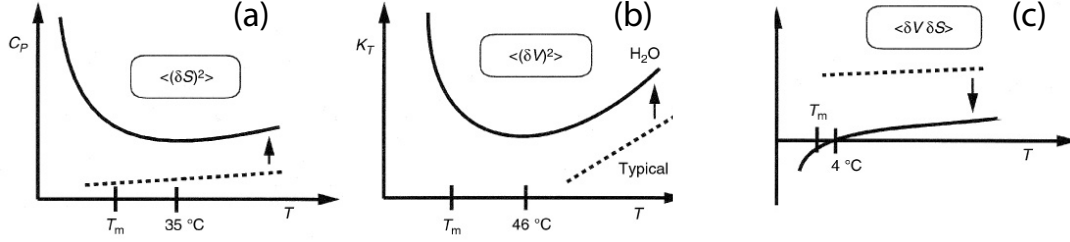
Figure 1.4: Anomalous behavior of water

Dashed curves are representative of typical liquids, while solid curves are quali-
tative estimates of water's behavior. The unexpected divergence of water's ther-
modynamic quantities is one reason behind suspecting the existence of a second
critical point C'. The text boxes show the fluctuations that are related to the
given thermodynamic quantity. From [32].

Water exhibits many uncommon thermodynamic properties, mostly due to
hydrogen bonding. One familiar property is a density maximum (corresponding
to a zero in α_P) at 4°C. It is also well-known that the liquid state is denser than the
usual solid state (Ice I_h) since ice floats. This is uncommon, as most substances
continually shrink upon cooling, shown by a positive thermal expansion coefficient
- see Figure 1.4 part (c). Though data are missing for lower temperatures due to
crystallization, α_P can be fit by a power law which surprisingly suggests that it
diverges to infinity around 228 K [33].

Each of the response functions can be associated with a corresponding fluctu-
ation [16]:

$$\langle(\delta V)^2\rangle = VkTK_T, \quad \langle(\delta S)^2\rangle = Nkc_P, \quad \langle(\delta S\delta V)\rangle = VkT\alpha_P \qquad (1.5)$$

where N is always fixed and $V = \langle V\rangle$. For any quantity Q, the fluctuations
in Q, $\langle(\delta Q)^2\rangle$, can be thought of as the standard deviation in Q, which is easily
calculated by $\sigma_Q^2 = \langle Q^2\rangle - \langle Q\rangle^2$. $\langle(\delta S\delta V)\rangle$ measures the correlation of volume and

entropy fluctuations; it is positive if the fluctuations are correlated, 0 if they are perfectly uncorrelated, and negative if they are anti-correlated. In typical liquids, fluctuations in volume and entropy decrease upon cooling, while the opposite happens in water. Fluctuations in volume and entropy are positively correlated in typical liquids, while in water they become negatively correlated below the temperature of maximum density (4° C at atmospheric pressure). This means a decrease in volume will increase the entropy, which is a consequence of hydrogen bonding. This is because the highly ordered, low entropy tetrahedral shapes found in supercooled water take up more space than unordered arrangements.

These effects are exaggerated as the temperature is lowered, and all three response functions are expected to diverge in the vicinity of 228 K [33]. See Figure 1.4 (a) and (b). This is what would be expected were water to have a liquid-liquid critical point, though it is not proof. The reason for such divergences is easy to see on a $P - V$ diagram. At a critical point, such as along the $T = 1$ isotherm in Figure 1.2, the slope dP/dV is flat, and thus K_T is infinite. Along isotherms of $T \gtrsim 1$, the response functions have huge maxima, though the functions no longer diverge. The locations of such maxima are known as Widom lines. Each response variable has a corresponding Widom line leaving a critical point, and the various Widom lines need not coincide. See Figure 1.7.

The liquid-gas critical point C of water is located at $T_C = 647$ K and $P_C = 22$ MPa (see Figure 1.5). Water is stable as a gas above the boiling line T_b, which is $T = 377$ K at atmospheric pressure, and water is stable as a crystal below the melting line T_m, which is $T = 273$ K at atmospheric pressure; see Figure 1.1. On a $T - P$ diagram, the melting line of water is negatively sloped until about 200 MPa, at which point is becomes positively sloped like most liquids. This accounts for pressure-induced melting of ice if the temperature is just below freezing.

Water can be supercooled at atmospheric pressure to approximately 235 K, at which point it homogeneously nucleates into a crystal regardless of the sample size or purity. The homogeneous nucleation temperature is shown by the curve T_h on Figure 1.5. If water is quenched (cooled rapidly) to a temperature below T_g, it can "bypass" crystallization and become a glass, meaning that it no longer

crystallizes within observable times. If water is quenched at atmospheric pressure, it forms a low density glass known as LDA. There is actually a range of forms of glassy water at atmospheric pressure; for simplicity, we categorize them all as LDA (it is expected that they are all of the same phase). Upon compression, LDA can form a distinct phase of glass with density roughly 30% greater, known as HDA [22]. Likewise, HDA can be decompressed and turn into LDA. There may also be a distinct form of HDA called VHDA, for very high density amorphous solid, but it is not know whether this is a distinct form or whether the change from HDA to VHDA is continuous [34, 16]. Part of the difficulties of probing glasses is that they are non-equilibrium materials, meaning that their properties depend on how they are formed. Hence HDA formed by compressing LDA shows slightly different properties than HDA formed by quenching compressed liquids. Upon heating either form of the glass, enough mobility is gained at T_X such that the liquid can relax to form a crystal. This occurs around 150 K, though depends on pressure (see Figure 1.5).
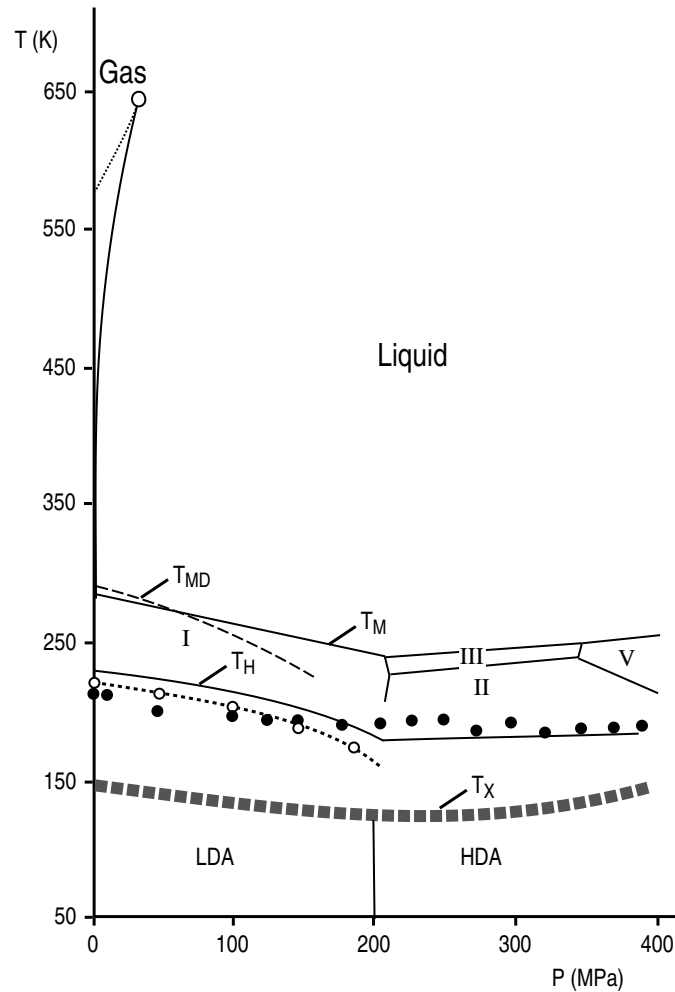
Figure 1.5: Known phase diagram of water

The liquid-gas critical point, C, is shown by the large open dot at $T = 647$ K. The unlabeled solid line is the liquid-gas coexistence line and the unlabeled dotted line leaving the critical point is the liquid-gas spinodal line. T_{MD} is the line of maximum density, and is 4°C at atmospheric pressure. The Roman numerals refer to polymorphs of ice; common ice is a type of ice I. The solid line at 200 MPa is the LDA-HDA coexistence line. Not show are the LDA-HDA and HDA-LDA spinodals. The ∘ are the loci of extrapolated singularities of K_T and the • are the loci of extrapolated singularities of D^{-1} (D is the translational diffusion constant, to be defined in the next section) From [32].
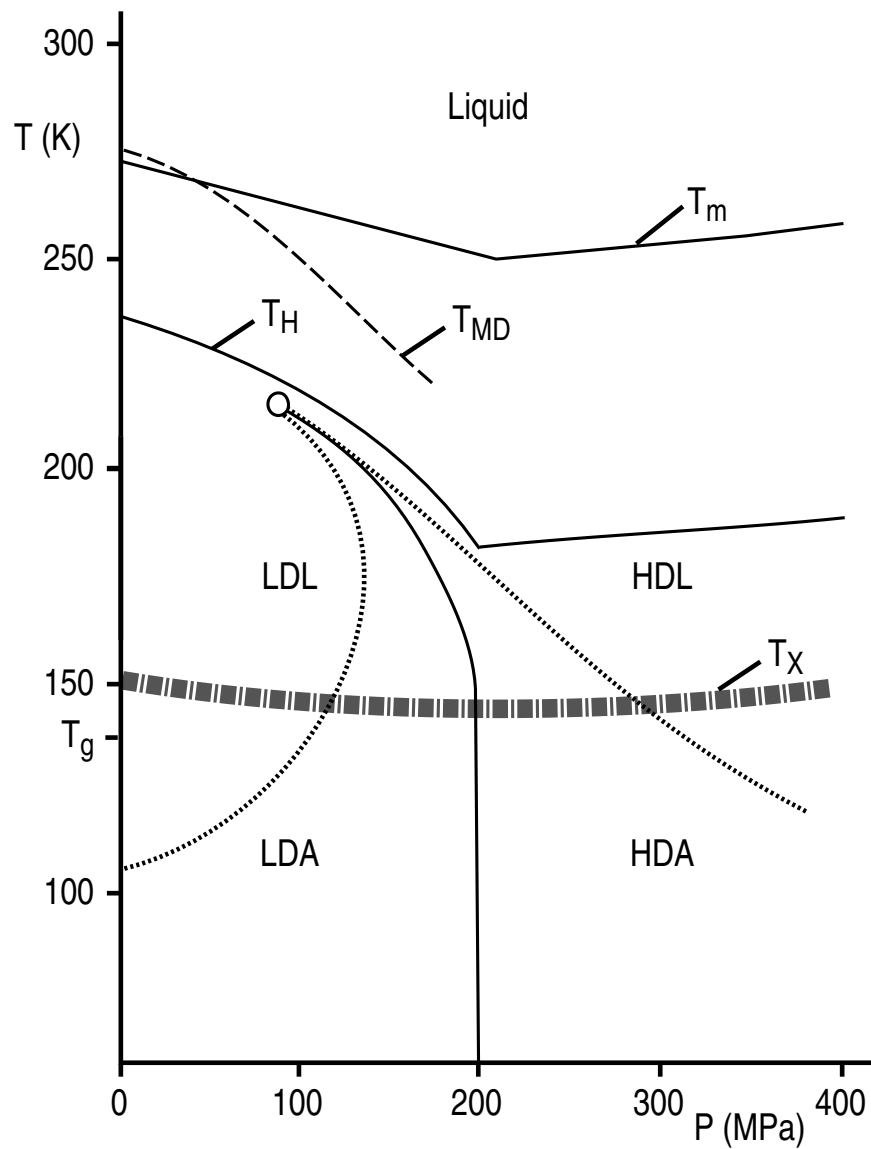
Figure 1.6: Proposed phase diagram of water according to liquid-liquid transition hypothesis

The ◯ is the liquid-liquid critical point C'. The solid line leaving the critical point is the LDA-HDA coexistence line, and the dashed lines are the LDA-HDA and HDA-LDA spinodals. The region of temperatures below T_H and above T_X is difficult to study and experiments at C' cannot be performed. From [32]
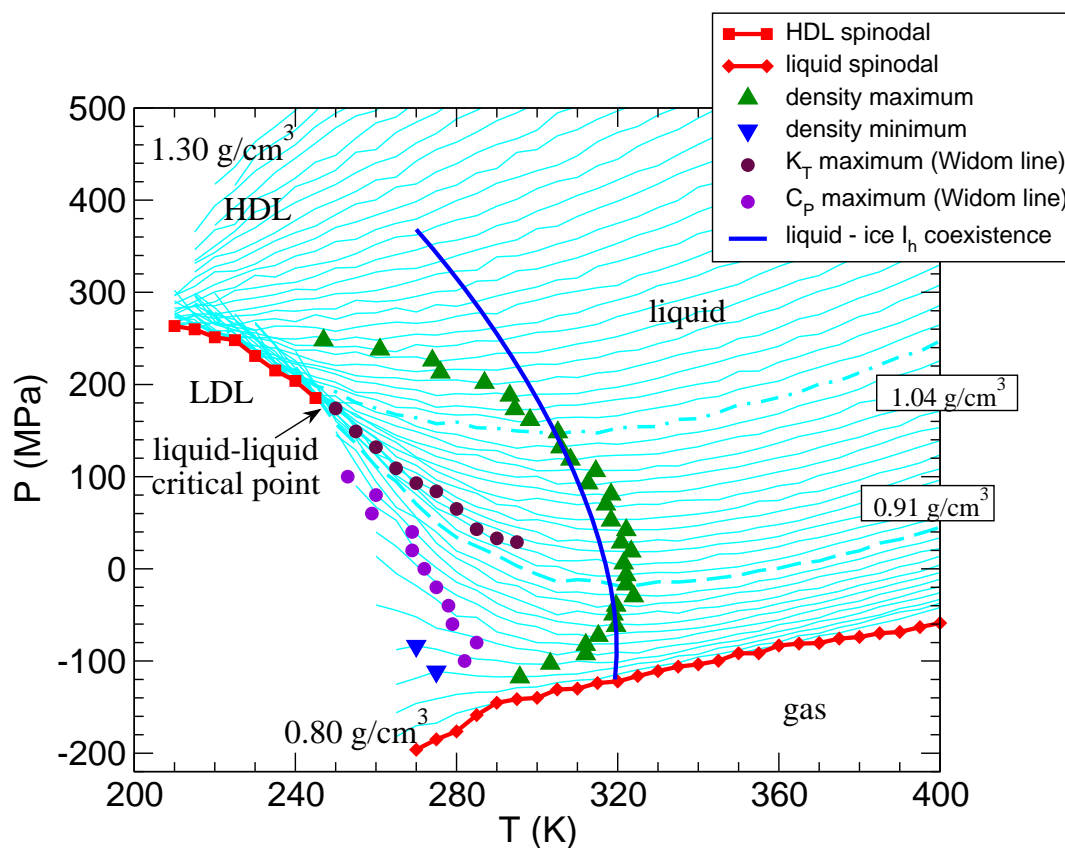
Figure 1.7: Phase diagram for ST2

The experimentally known phase diagram for ST2 water. In general, thermodynamic events in ST2 water happen roughly 30 K and 80 MPa higher than in real water. The liquid-gas spinodal is shown, as well as one of the spinodals from the liquid-liquid critical point. The K_T maxima indicate the K_T Widom line, and the C_P maxima indicate the C_P Widom line; the K_T and C_P Widom lines are distinct and do not fall on isochores. Data from P.H. Poole (private communication).

1.3   Dynamics

1.3.1   Mean-Squared Displacement

As state earlier, the aim of this thesis is to characterize dynamic properties of su-
percooled water. Dynamical quantities can be described by microscopic variables
based on the positions $\{r_i\}$ and velocities $\{v_i\}$ of all the particles. One of the
most fundamental dynamical variables is the mean-squared displacement (MSD)

$$\langle r^2(t)\rangle \equiv \langle |\boldsymbol{r}(t+t_0) - \boldsymbol{r}(t_0)|^2\rangle, \tag{1.6}$$

where the brackets denote averaging over all N particles and over all times t_0 [35].
In this thesis, the mean squared displacement always refers to the displacement
of the oxygen atom. An example of $\langle r^2(t)\rangle$ is show in Figure 1.8 part (a).

When tracking the motion of a single particle, the particle at first moves
without hitting other particles and the motion is said to be ballistic because
$r = v_{rms}t$, hence $r^2 \propto t^2$ so we expect the MSD to have a slope of 2 on a log-log
plot. At intermediate times, the particle starts colliding with other particles. At
high temperatures, the particle begins diffusive motion and the log-log slope is 1.
At lower temperatures, the particle may be "caged-in" and will take much longer
before it begins to diffuses.

The positions and velocities of all $3N$ atoms determine a set of N solid an-
gles, $\{\boldsymbol{\phi}_i\}$, and angular velocities, $\{\boldsymbol{\omega}_i\}$. We define the rotational mean-squared
displacement $\langle\phi^2(t)\rangle$ (referred to as the rotational MSD) to be

$$\langle\phi^2(t)\rangle \equiv \langle |\boldsymbol{\phi}(t+t_0) - \boldsymbol{\phi}(t_0)|^2\rangle \tag{1.7}$$

but need to carefully define the angular coordinates by

$$\boldsymbol{\phi}(t+t_0) - \boldsymbol{\phi}(t_0) = \int_{t_0}^{t'} \boldsymbol{\omega}(t')dt' \tag{1.8}$$

because $\boldsymbol{\phi}$ itself is limited to values on the unit sphere and we don't want to
limit the rotational changes to unit sphere values. $\langle\phi^2(t)\rangle$ shows qualitatively

similar behavior to $\langle r^2(t) \rangle$, but the form of the time and temperature dependence is quantitatively different.

The translational self-diffusion constant, written as D or D_{trans}, measures the rate at which particles diffuse. A higher value corresponds to increased mobility, and hence for most liquids D_{trans} will decrease upon application of pressure or cooling. Likewise, D_{rot} measures the "diffusion" of the angle of a particle. The Einstein relation

$$D_{trans} = \lim_{t \to \infty} \frac{\langle r^2(t) \rangle}{6t} \tag{1.9}$$

and the Debye-Einstein relation

$$D_{rot} = \lim_{t \to \infty} \frac{\langle \phi^2(t) \rangle}{4t} \tag{1.10}$$

give methods for determining the translational and rotational diffusion constants D_{trans} and D_{rot} from the respective mean squared displacements [35]. The behavior of a substance is called "diffusive" when $\langle r^2(t) \rangle / t$ is constant (i.e. a slope of one on a log-log plot of the mean square displacement) and thus D can be calculated without requiring that $t \to \infty$.

The Stokes-Einstein (SE) approach allows one to relate mass transport, measured by diffusion constants, to momentum transport, measured by viscosity η. If one assumes spherical molecules, the SE equation predicts

$$D_{trans} = \frac{k_B T}{\gamma \pi d \eta}, \quad i.e. \frac{D_{trans} \eta}{T} = \text{constant} \tag{1.11}$$

where γ is either 2 or 3, depending on if "slip" or "stick" conditions hold (see [36]). Similarly, the Debye-Stokes-Einstein (DSE) equation predicts

$$D_{rot} = \frac{3k_B T}{\gamma \pi d^3 \eta}, \quad i.e. \frac{D_{rot} \eta}{T} = \text{constant.} \tag{1.12}$$

Even though water is not spherical and is in a discrete medium, the SE and DSE equation hold remarkably well over a wide range of temperatures. However, because the geometry of water is different, these relationships are not intended to be quantitative, though they can often be within a factor of 2 [16]. The equations
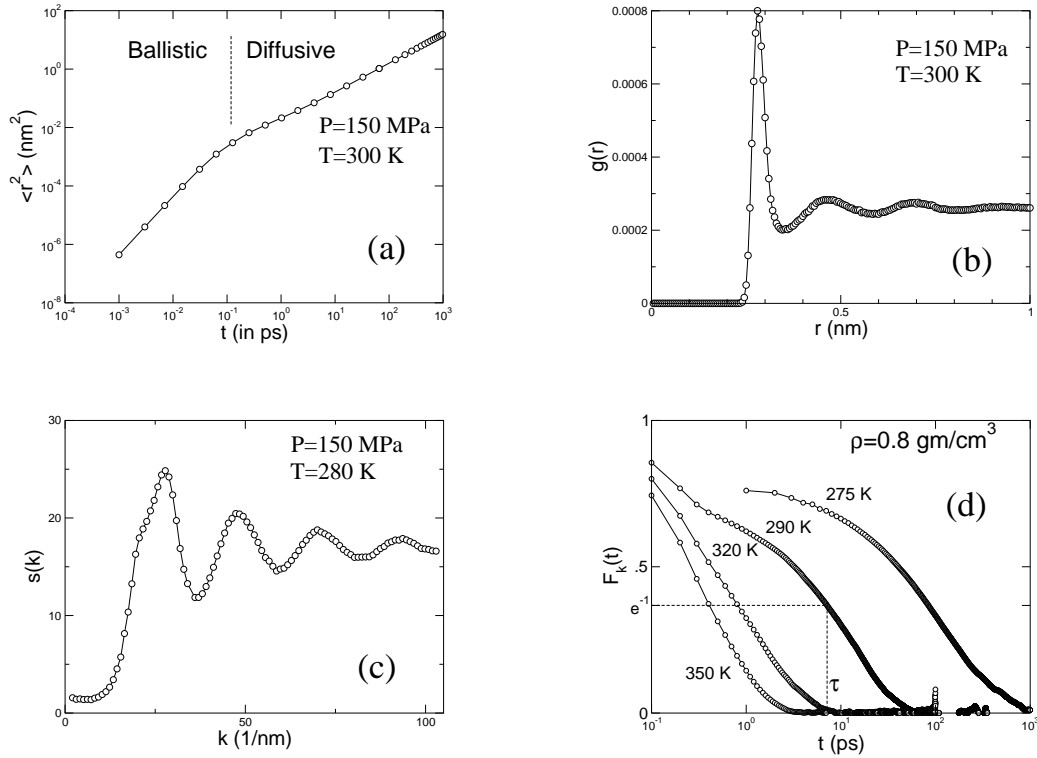
Figure 1.8: Response functions

(a) is the mean-squared displacement at a high temperature; (b) is the radial distribution function; (c) is the static structure factor; (d) is the intermediate scattering function at various temperatures

predict that D_{trans}/D_{rot} should be independent of T, and this is true experimentally when $T > T_m$ for most low-viscosity liquids. Recent experimental work has suggested that the SE equation breaks down near T_g (see the final section in chapter 3); the data collected in this thesis allow us to test the SE and DSE equations.

1.3.2   Correlation Functions

Correlation functions typically measure either correlations in space, time, or a mixture of the two. The radial distribution function, $g(r)$, is proportional to the

probability of finding two molecules a distance $r = |\boldsymbol{r}|$ apart, and is one of the simplest measures of spatial correlation. See Figure 1.8 part (b). We compute $g(r)$ by [37]

$$g(r) = \frac{V}{N^2} \left\langle \sum_{i=1}^{N} \sum_{j \neq i}^{N} \delta(\boldsymbol{r} - \boldsymbol{r}_{i,j}) \right\rangle \tag{1.13}$$

The location of the first peak in $g(r)$ is the distance to the first nearest neighbor. While $g(r)$ cannot be directly measured experimentally, the Fourier transform of $g(r)$,

$$S(\boldsymbol{k}) = 1 + \rho \int e^{-i\boldsymbol{k}\cdot\boldsymbol{r}} g(r) d\boldsymbol{r}, \tag{1.14}$$

known as the (static) structure factor, can be measured in x-ray or neutron scattering experiments; see Figure 1.8 part (c). Hence $g(r)$ can be obtained by Fourier transforming $S(\boldsymbol{k})$. The structure factor can also be expressed as

$$S(\boldsymbol{k}) = \frac{1}{N} \langle \rho_{\boldsymbol{k}} \rho_{-\boldsymbol{k}} \rangle \tag{1.15}$$

where

$$\rho_{\boldsymbol{k}} = \sum_{i=1}^{N} e^{-i\boldsymbol{k}\cdot\boldsymbol{r}_i}. \tag{1.16}$$

The van Hove function, $G(\boldsymbol{r}, t)$, measures the probability of finding a particle at a position r at a time t given that there was a particle at an arbitrary origin $r = 0$ at time $t = 0$, and is given by

$$G(\boldsymbol{r}, t) = \frac{1}{N} \left\langle \sum_{i=1}^{N} \sum_{j=1}^{N} \delta \left[\boldsymbol{r} + \boldsymbol{r}_j(0) - \boldsymbol{r}_i(t) \right] \right\rangle \tag{1.17}$$

$G(\boldsymbol{r}, t)$ is a t-dependent generalization of $g(r)$.

The intermediate scattering function is defined by the Fourier transform of the van Hove function:

$$F_{\boldsymbol{k}}(t) = \frac{1}{N} \frac{1}{S(\boldsymbol{k})} \langle \rho_{\boldsymbol{k}}(t) \rho_{-\boldsymbol{k}}(0) \rangle = \frac{1}{S(\boldsymbol{k})} \int G(\boldsymbol{r}, t) e^{-i\boldsymbol{k}\cdot\boldsymbol{r}} d\boldsymbol{r}. \tag{1.18}$$

The intermediate scattering function can be measured by neutron scattering. Note that $F_{\boldsymbol{k}}(0) = 1$ and $F_{\boldsymbol{k}}(\infty) = 0$. In this thesis, we look at the dependence of $F_{\boldsymbol{k}}(t)$ on time, keeping $\boldsymbol{k}$ fixed (using the value at the first peak of $S(\boldsymbol{k})$). The quantity we actually study is $F_k(t)$, which is $F_{\boldsymbol{k}}(t)$ averaged over all $|\boldsymbol{k}| = k$. From this, we can define a relaxation time τ_α by the time such that $F_k(\tau_\alpha) = e^{-1}$. This relaxation time is a bulk property (since we average the intermediate scattering function over all particles), and we expect that it is proportional to the shear viscosity η. It is possible to calculate η but it requires storing information on velocity as well as position, which we did not record. Further extensions of this work will calculate η and presumably verify that it is proportional to τ_α. Experimentalists measure η and not τ_α.

1.3.3   Rotational Variables

If $\boldsymbol{u}_i$ is a unit vector associated with each molecule i (for example, the normalized dipole vector), then the dipole-dipole correlation functions are defined

$$C_l(t) = \langle P_l(\boldsymbol{u}_i(t) \cdot \boldsymbol{u}_i) \rangle \tag{1.19}$$

where P_l is the lth Legendre polynomial [35]. The dipole-dipole correlation functions are defined in terms of the Legendre polynomials because C_1 can be determined by the spectral bandshapes of infrared absorption and C_2 can be determined by Raman scattering [35]. We measure C_1 and C_2 and focus on C_2, as this is the most commonly measured rotational variable in experiments.

Associated with C_l is a characteristic time τ_l, either defined as the integral of C_l over all time or as the time it takes C_l to decay to e^{-1} of its original value, in analogy to τ_α. Both definitions are expected to show the similar temperature dependence. We use the latter definition because it does not require short-time data to calculate. Figure 1.9 compares the two definitions of τ_l.
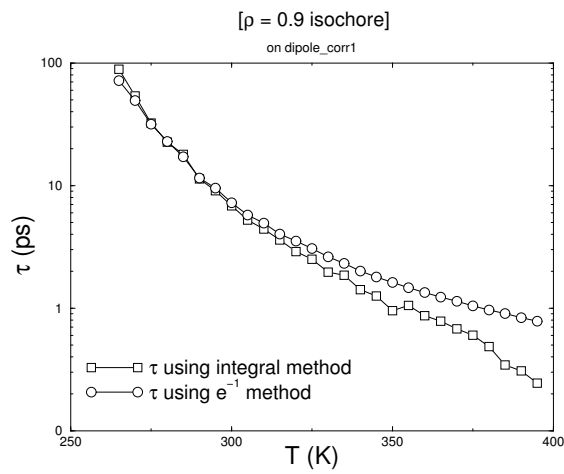
Figure 1.9: Rotational time constant

Shown are two definitions of τ_l; they disagree at high T because the integral-dependent definition becomes more sensitive to short-times, and data were not collected at intervals less than 100 fs. $l=1$, $\rho = 0.8\,\text{g/cm}^3$

1.3.4 Arrhenius Behavior

At high temperatures, diffusion constants and time constants are expected to follow Arrhenius behavior [16]. Specifically, this means that at a fixed pressure,

$$\tau_\alpha = \tau_0 e^{E/kT} \tag{1.20}$$

where τ_0 is a constant, k is Boltzmann's constant, and E is an activation energy that varies across pressure but is not expected (in the simplest models) to vary across temperature. As temperature lowers, the relaxation time increases exponentially due to reduced momentum transport.

It has been known for many years that such relations do not hold for sufficiently cold water [16]. Below a certain temperature $T_A = T_A(P)$, we expect non-Arrhenius behavior of the form

$$\tau_\alpha = \tau_0 e^{E/k(T-T_0)} \tag{1.21}$$

where T_0 is a non-zero temperature at which T_α diverges to infinity. In other words, $T_0 = 0$ in the Arrhenius case, and τ_α does not diverge at positive temperature. Our results show such non-Arrhenius behavior and we try to characterize T_A in section 3.1.3.

We also expect "caging" phenomena to become significant at lower temperature. This is expected from previous simulations and we confirm this; caging is discused in Section 3.1.

1.3.5 Spatially Heterogeneous Dynamics

The idea that dynamics in liquids are spatially homogeneously distributed has been implicit so far in this work as well as in much of the standard liquid theory. However, in the 1990s, as a means to explain enhanced translational diffusion, some authors (see [38]) suggested that liquids are not spatially homogeneous at low temperatures. Instead, heterogeneous pockets of more mobile liquids fluctuate in and out of existence. There have been several flavors of theories about the

characterization of the heterogeneities (see the review papers [39, 38]), but the simplest of them explain the enhanced translational diffusion as follows, due to [40]: suppose that, at any given time, every local region of water is in either a fast state, with $\tau_2 = \tau_{fast}$, or in a slow state, with $\tau_2 = \tau_{slow}$, and to simplify further, assume that half the liquid is in a fast state and half is in a slow state. We also assume that the SE and DSE equations are obeyed locally in each region. Each region is also characterized by a translational diffusion constant D which can take the values D_{fast} or D_{slow}. Then, in our example, $\tau_2 = (\tau_{slow} + \tau_{fast})/2$ and $D = (D_{slow} + D_{fast})/2$. If $\tau_{fast} \ll \tau_{slow}$ and $D_{fast} \gg D_{slow}$, then $\tau \approx \tau_{slow}/2$ and $D \approx D_{fast}/2$. The stronger the heterogeneities, the more D is enhanced by the D_{fast} region, while τ_2 remains coupled to τ_{slow}. To put it simply: the correlation time is dominated by the slow regions, while the diffusion constant is dominated by the fast regions.

Regardless of the motivation that first suggested water was spatial heterogeneous, recent work has conclusively shown, using both experiments and computer simulations, that heterogeneities do exist [39, 38].

1.4 Computer Models

Computer simulation offers advantages over real-world experiments. Samples are of course pure, and thermodynamic variables can be rigidly controlled. The actual positions and velocities for each particle can be recorded, allowing, in theory, calculation of any desirable classical dynamical or thermodynamical quantity.

There are also drawbacks to using computer simulations. One major such drawback is due to approximations in calculating the intermolecular potential. Different approximates lead to different models of water. The computer simulations in this work used the "ST2" model for water, and therefore the results only apply exactly to ST2 water [41]. However, ST2 water has been studied for over 30 years and shows qualitatively similar behavior to water, such as exhibiting a temperature of maximum density and showing phase transitions near their actual location. Quantitatively, ST2 often places events at higher temperatures. For ex-

ample, real water has a maximum density of $\rho = 1$ g/cm^3 along the $P = 0.1$ MPa isobar, with a temperature of maximum density (TMD) at 277 K = 4°C. In ST2, a maximum density of $\rho = 1$ g/cm^3 is attained along the 82 MPa isobar, and at a temperature of 312 K = 37°C [6]. There is also evidence that the melting temperature is elevated over that of real water [42]. These higher temperatures and densities are due to the overemphasis of tetrahedral structure in the ST2 potential. The tendency to form tetrahedral molecular arrangements is associated with anomalous properties. The artificial tetrahedral form of the ST2 potential creates tetrahedral molecular arrangements at higher temperatures than is possible in real water. While this is a disadvantage in terms of quantitative results, it is an advantage in other ways, since lower temperatures are costly in terms of computing time. Modelling ST2 at 250 K may provide a good description of water at 220 K, without having to run simulations at 220 K (which take orders of magnitude more time to equilibrate than simulations at 250 K). In general, by subtracting 30 to 40 K from temperatures shown in ST2 behavior, we get a crude estimate of the temperature of the same behavior in water. In this thesis, I use the words "water" and "ST2 water" interchangeably, with the implicit assumption that they are not expected to be identical.

There are other standard simulation models, and there is evidence that water's behavior is often found "sandwiched" by various models, that is, one model may overestimate a quantity Q and another model may underestimate Q. In this way computer models can define upper and lower bounds on the properties of real water. ST2 is discussed in detail in the next chapter. Details on other water molecules can be found in [43] for the SPC/E model, in [44] for the TIP4P model and in [45] for the TIP5P model.

Other drawbacks of computer simulation are due to constraints in processing power. "Computational experiments" simulate only nanoseconds or less, but may take days to run. Lower temperatures equilibrate slower and therefore simulations must last longer. This means there is an effective limit to how low in temperature water can be simulated. Specifically, this means equilibrium properties with relaxation times $\gtrsim 1\,\mu$s cannot be probed well by simulation. Increases in processing

speeds increase the range of temperatures where water and other liquids can be simulated, and thus every year water can be studied to lower temperatures.

There are other undesirable effects of simulation that are introduced by various simulation techniques. Some of these techniques are practically essential for studying bulk liquids (like periodic boundary conditions) and others are merely convenient time-savers (like using potential truncation) but still important. The following chapter on computer simulation will cover these techniques and what can be done to minimize unphysical effects.

1.5 Computational Resources

The purpose of this thesis is to investigate the dynamic properties of supercooled liquid water. To do this, ST2 water was simulated on computers. The computing framework at Wesleyan University was a Beowulf cluster of 50 processors running LINUX with the MOSIX add-on. With MOSIX, programs jobs are distributed transparently to the cluster via a central computer. Each processor had a clock speed of around 3 GHz, and had from 512 MB to 4 GB of RAM. File storage was centrally shared in a RAID 5 1.2 TB hard drive system. Code was written exclusively in C.

Additional computation was done on a computer cluster at St. Francis Xavier University in Nova Scotia. The cluster had 90 dual-CPU Opteron machines running SunOS. The simulation code was written in Fortran and analysis codes were written in C. Most of the data presented in this thesis are the result of a series of two-day simulations on this cluster, which used equilibrated configurations that had been previously simulated over many days. These data were subsequently analyzed on both clusters.

The actual simulation code was adapted from existing code. The C-code on the Wesleyan cluster was based off the Fortran code on the Nova Scotia computer cluster, and previous work has shown the two codes to be satisfactorily similar. Contributers and original authors of the code include Alfons Geiger, Francesco Sciortino, Peter Poole, Stephen Harrington, and Francis Starr. The C-codes were

compiled using the GNU gcc compiler with the maximum possible optimization.

The main data were a series of 1,233 computer simulations run at various fixed temperatures and volumes (i.e. densities) which took up 989 GB of hard disk space. Subsequent analysis produced about $30,000$ files taking up 733 MB. The densities ranged from 0.80 g/cm^3 to 1.20 g/cm^3 in steps of .01 g/cm^3. Along these isochores, simulations were run at temperatures from 250 to 400 K in 5 K intervals, though not all isochores were run at the lowest temperature; see Table 1.1. At each temperature and pressure, a preliminary run was performed until it reached equilibration. In practice, the runs were simulated for the longer of the time needed for the mean-squared displacement to reach 1 nm^2 or 100 ps. Each preliminary run used the final configurations of a run at higher temperature as its starting configuration, except for the 400 K runs which were started using regularly spaced positions and quasi-random velocities chosen from the Maxwell-Boltzmann distribution. Using the final configurations of the equilibrium run, a production run was started and run until the same set of criteria was reached.

At some of the lowest temperatures and isochores, the mean-squared displacement did not show diffusive behavior even after it reached 1 nm^2, and thus the diffusion constants for these runs were not included in the analysis. The simulation code used a time step of 1 fs, and the positions of all the atoms were written to disk every 100 fs. These configuration files exceed 12 GB for the longest runs, and because this exceeds the RAM capabilities of the clusters, these files had to be reduced to an effective spacing of 1 or 2 ps. Thermodynamic data were calculated at the run-time of the experiment, while the dynamical variables D_{trans}, D_{rot}, C_1, C_2 and $F_k(t)$ were calculated at later times. Specifically, the pressure for each run was recorded which gave a mapping from statepoints (T,ρ) to statepoints (T,P). Isobars of a quantity Q were calculated by fitting splines to isotherms of Q as a function of P, then taking the value of the spline at 50 MPa intervals.

ρ\T	250	255	260	265	270	275	280	285	290	295	300	305	310	315	320	325	330	335	340	345	350	355	360	365	370	375	380	385	390	395	400
80							2452.1	1075.7	630.2	352.7	239.3	167.7	110.7	100	100	100	100	100	100	100	100	100	100	100	100	100	100	100	100	100	100
81							2326.1	1209.7	591.7	371.9	209.9	153.3	107.2	100	100	100	100	100	100	100	100	100	100	100	100	100	100	100	100	100	100
82						4502.1	1827.1	1019.3	527.8	343.7	220.9	141.3	113.5	100	100	100	100	100	100	100	100	100	100	100	100	100	100	100	100	100	100
83						4226.1	2072.1	918.5	486.6	299.4	182.4	105.4	100	100	100	100	100	100	100	100	100	100	100	100	100	100	100	100	100	100	100
84						3177.1	1637.1	802.6	477.2	279.2	205.4	142	100	100	100	100	100	100	100	100	100	100	100	100	100	100	100	100	100	100	100
85						2082.1	1172.5	690.6	448.5	272.3	198.2	142.9	100.3	100	100	100	100	100	100	100	100	100	100	100	100	100	100	100	100	100	100
86				3896.1	2171.1	948.4	592	358.4	217.7	155.3	128.8	100	100	100	100	100	100	100	100	100	100	100	100	100	100	100	100	100	100	100	100
87				2690.1	1237.1	786.9	525	305.5	186.5	154.9	117.7	100	100	100	100	100	100	100	100	100	100	100	100	100	100	100	100	100	100	100	100
88			3462.1	1688.1	912.5	365.6	235.4	180.3	149.6	106.6	100	100	100	100	100	100	100	100	100	100	100	100	100	100	100	100	100	100	100	100	100
89		3512.1	2264.1	1235.3	817.2	491.9	386.8	296	243.2	188.7	137.8	105.3	100	100	100	100	100	100	100	100	100	100	100	100	100	100	100	100	100	100	100
90		2197.1	1604.1	820.9	578	386.8	296	218.5	149.8	123.5	100	100	100	100	100	100	100	100	100	100	100	100	100	100	100	100	100	100	100	100	100
91	2772.1	1740.1	1097.1	694.4	503	386.8	322.3	241.6	186.7	143.7	113.3	100	100	100	100	100	100	100	100	100	100	100	100	100	100	100	100	100	100	100	100
92	1961.1	1288.1	838.6	558.3	404	279.6	212.2	171.3	128	101	100	100	100	100	100	100	100	100	100	100	100	100	100	100	100	100	100	100	100	100	100
93	1372.1	645.3	486.5	348.4	253.2	184.9	152.3	130	100	100	100	100	100	100	100	100	100	100	100	100	100	100	100	100	100	100	100	100	100	100	100
94	1190.8	802.6	542.2	396.6	303	230.2	165.9	135.3	118.8	100.4	100	100	100	100	100	100	100	100	100	100	100	100	100	100	100	100	100	100	100	100	100
95	988.4	613.9	476.4	357.6	269.5	203.7	166	131.7	111.1	100	100	100	100	100	100	100	100	100	100	100	100	100	100	100	100	100	100	100	100	100	100
96	762.3	531.9	385.1	301.4	223.6	189.7	161.3	125.7	108.6	100	100	100	100	100	100	100	100	100	100	100	100	100	100	100	100	100	100	100	100	100	100
97	642.5	488.1	371.3	279.5	206.5	173.4	145.4	115.6	100	100	100	100	100	100	100	100	100	100	100	100	100	100	100	100	100	100	100	100	100	100	100
98	587.5	453	326.8	267.7	204	156.9	122.1	109.6	100.3	100	100	100	100	100	100	100	100	100	100	100	100	100	100	100	100	100	100	100	100	100	100
99	517.8	378.8	313.1	241.5	178	155.1	126.8	101.7	100	100	100	100	100	100	100	100	100	100	100	100	100	100	100	100	100	100	100	100	100	100	100
100	459.4	359	270.6	216.4	172.4	160.5	135.6	111.5	103.5	100	100	100	100	100	100	100	100	100	100	100	100	100	100	100	100	100	100	100	100	100	100
101	422	326	252.8	193.1	160.5	152.8	110.9	100	100	100	100	100	100	100	100	100	100	100	100	100	100	100	100	100	100	100	100	100	100	100	100
102	366.7	305.9	233	180.3	159.4	135.7	113.3	100	100	100	100	100	100	100	100	100	100	100	100	100	100	100	100	100	100	100	100	100	100	100	100
103	328.7	257.3	207.5	184.8	145.9	135.1	123.7	107.7	100	100	100	100	100	100	100	100	100	100	100	100	100	100	100	100	100	100	100	100	100	100	100
104	337.3	243.2	211.9	176.5	141.8	134.7	127.1	104.7	100	100	100	100	100	100	100	100	100	100	100	100	100	100	100	100	100	100	100	100	100	100	100
105	315.1	250.5	209.1	175.7	134.7	126.6	110.5	100	100	100	100	100	100	100	100	100	100	100	100	100	100	100	100	100	100	100	100	100	100	100	100
106	296.3	232.8	197.1	157.1	134.8	117.1	102.5	100	100	100	100	100	100	100	100	100	100	100	100	100	100	100	100	100	100	100	100	100	100	100	100
107	289.9	226.1	188.5	151.4	132.1	114.5	100	100	100	100	100	100	100	100	100	100	100	100	100	100	100	100	100	100	100	100	100	100	100	100	100
108	255.5	227.1	179.2	151.2	123.1	107	100	100	100	100	100	100	100	100	100	100	100	100	100	100	100	100	100	100	100	100	100	100	100	100	100
109	266.4	197	183.8	153.4	133.7	111.5	100	100	100	100	100	100	100	100	100	100	100	100	100	100	100	100	100	100	100	100	100	100	100	100	100
110	246.4	213.2	161.2	153.1	123.7	110.8	100	100	100	100	100	100	100	100	100	100	100	100	100	100	100	100	100	100	100	100	100	100	100	100	100
111	265.6	221.5	170.6	147.6	129	123.8	100.1	100	100	100	100	100	100	100	100	100	100	100	100	100	100	100	100	100	100	100	100	100	100	100	100
112	252.7	217.7	162.4	149.7	123.8	110.1	100	100	100	100	100	100	100	100	100	100	100	100	100	100	100	100	100	100	100	100	100	100	100	100	100
113	244	204.8	177.3	150.8	131.8	104.3	100	100	100	100	100	100	100	100	100	100	100	100	100	100	100	100	100	100	100	100	100	100	100	100	100
114	246.3	203.7	171.6	142.2	128.2	104.5	100	100	100	100	100	100	100	100	100	100	100	100	100	100	100	100	100	100	100	100	100	100	100	100	100
115	249.1	204.5	160	145.8	120.9	102.9	100	100	100	100	100	100	100	100	100	100	100	100	100	100	100	100	100	100	100	100	100	100	100	100	100
116	235.5	202.8	168.5	146.4	122.1	106.1	100	100	100	100	100	100	100	100	100	100	100	100	100	100	100	100	100	100	100	100	100	100	100	100	100
117	232.3	201.3	158.6	141	121.2	109.2	100	100	100	100	100	100	100	100	100	100	100	100	100	100	100	100	100	100	100	100	100	100	100	100	100
118	250.5	209.2	171.3	158.4	132.7	110.8	100	100	100	100	100	100	100	100	100	100	100	100	100	100	100	100	100	100	100	100	100	100	100	100	100
119	268	198.6	183.3	153	125.7	116.6	100	100	100	100	100	100	100	100	100	100	100	100	100	100	100	100	100	100	100	100	100	100	100	100	100
120	256.7	202.7	178	157.6	135.5	116	100	100	100	100	100	100	100	100	100	100	100	100	100	100	100	100	100	100	100	100	100	100	100	100	100

Table 1.1: Statepoints

Shown are the statepoints simulated. The leftmost column is density in 10^{-2} g/cm³ and the topmost row is temperature in K. The values of the table are the times in ps that the state point was simulated for during the production run

Chapter 2

Computer Simulation

2.1 ST2 Model

The main difficulty in creating an accurate model of water arises from defining the intermolecular potential. Water has dipole as well as higher multipole moments, and forms directional hydrogen bonds. Creating a model is a balance between incorporating the physics and having a quickly computable potential. One of the earliest and most used models of water is known as ST2, named after Stillinger [41], its originator. It models the electrostatic interactions of water by placing four fractional electric charges of magnitude q at predetermined sites in the molecule and also includes a Lennard-Jones term to account for the dispersion forces. Two $+q$ charges model the hydrogen atoms and are each located exactly 1 Å from the center of the oxygen molecule, at an angle θ_t apart, where θ_t is the tetrahedral angle $\theta_t = 2\cos^{-1}(3^{-1/2}) \simeq 109°28'$. Two $-q$ charges are placed $l = .8$Å from the center of the oxygen molecule and are also θ_t apart; see Figure 2.1. The value of q is .2357 $e = 3.77 \cdot 10^{-20}$ C. Because the fixed charges do not model a dipole perfectly, the electrostatic terms of the potential are multiplied by a switching function $S(r)$ with continuous first derivate which reduces the effect of the electrostatic terms when r is small (see Figure 2.2). The form of the switching function is
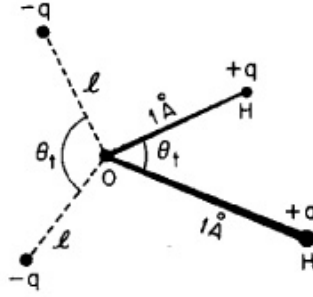
Figure 2.1: The structure of the ST2 model, from [41]. l is .8 Å

$$S(r) = \begin{cases} 0 & \text{if } r < R_L \\ \dfrac{(r - R_L)^2(3R_U - R_L - 2r)}{(R_U - R_L)^3} & \text{if } R_L \leq r \leq R_U \\ 1 & \text{if } r < R_U \end{cases} \tag{2.1}$$

There is also a 5th site force corresponding to the Lennard-Jones interactions the water molecules. The Lennard-Jones potential is

$$V_{LJ}(r) = 4\epsilon \left[\left(\frac{\sigma}{r}\right)^{12} - \left(\frac{\sigma}{r}\right)^{6} \right]. \tag{2.2}$$

ST2 uses the values $\epsilon = 5.2605 \cdot 10^{-22}$ Joules and $\sigma = 3.1$ Å. See Figure 2.3. The $(\sigma/r)^6$ term captures attraction due to van der Waals forces, while the $(\sigma/r)^{12}$ term provides core repulsion.

Because the point charges are in a fixed tetrahedral geometry, ST2 overemphasizes tetrahedral structure and does not reproduce expected liquid structure at high pressures. However, ST2 has been used for over 30 years and is believed to provide useful information about the dynamics and thermodynamics of water, especially when used in conjunction with other models, such as the SPC/E model, which significantly underemphasizes the tetrahedral structure of water.
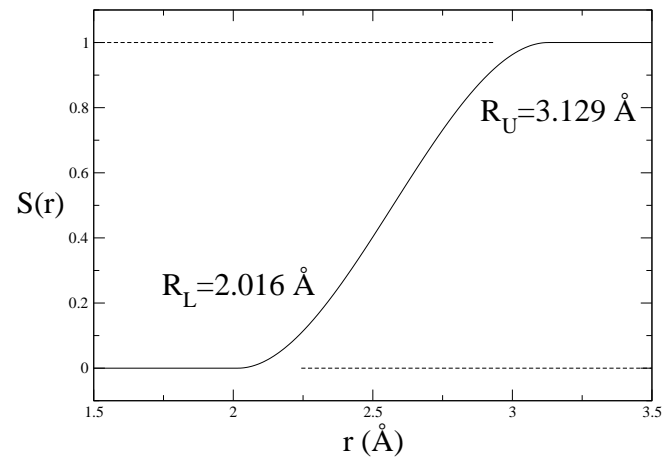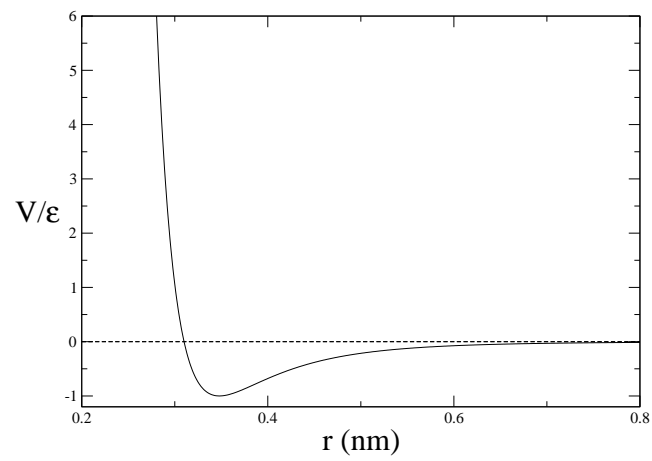
Figure 2.2: The switching function

Figure 2.3: The Lennard-Jones potential for the ST2 model

2.2   Molecular Dynamics

2.2.1   Integrating the Equations of Motion

Given an intermolecular potential, the problem of moving the particles still remains. The physics is simple; the force is the negative gradient of the potential, and Newton's second law relates force to acceleration. The acceleration defines the change in the velocities which in turn define the change in position. However, for a given timestep δt, we want to minimize error and calculation time. There are many finite-difference method algorithms to chose from, but the importance of quick calculation time makes many impractical. For our simulations, we used the "velocity Verlet" algorithm [37], which is of the form

$$\boldsymbol{r}(t + \delta t) = \boldsymbol{r}(t) + \delta t \boldsymbol{v}(t) + \tfrac{1}{2}(\delta t)^2 \boldsymbol{a}(t) \tag{2.3a}$$

$$\boldsymbol{v}(t + \delta t) = \boldsymbol{v} + \tfrac{1}{2}\delta t \left[\boldsymbol{a}(t) + \boldsymbol{a}(t + \delta t) \right] \tag{2.3b}$$

The typical value of δt for water is 1 fs.

The above calculations are performed for each atom in the simulation. Because we require that water stay in molecular form, it is necessary to maintain the intramolecular OH-bonds. This is done via constraint dynamics, and we use the SHAKE algorithm [37, 46], which assumes a fixed OH bond length of $d_{\alpha\beta} = 1 \,\text{Å}$. The idea of the process is that all atoms are free to move as if there were no intramolecular bonds. Then, after each time step, the SHAKE algorithm is applied which nudges the atoms until the OH-bonds are restored.

Specifically, after calculating the unconstrained positions $\boldsymbol{r}_{i\alpha}(t + \delta t)$, the positions are adjusted as follows:

$$\boldsymbol{r}'_{i\alpha}(t + \delta t) = \boldsymbol{r}_{i\alpha}(t + \delta t) + \frac{1}{2}\left(\frac{m_\alpha}{\mu}\right)^{-1} \frac{\delta r_{\alpha\beta}^2(t + \delta t) - d_{\alpha\beta}^2}{\delta \boldsymbol{r}_{\alpha\beta}(t + \delta t) \cdot \delta \boldsymbol{r}_{\alpha\beta}(t)} \delta \boldsymbol{r}_{\alpha\beta}(t) \tag{2.4a}$$

$$\boldsymbol{r}'_{i\beta}(t + \delta t) = \boldsymbol{r}_{i\beta}(t + \delta t) - \frac{1}{2}\left(\frac{m_\beta}{\mu}\right)^{-1} \frac{\delta r_{\alpha\beta}^2(t + \delta t) - d_{\alpha\beta}^2}{\delta \boldsymbol{r}_{\alpha\beta}(t + \delta t) \cdot \delta \boldsymbol{r}_{\alpha\beta}(t)} \delta \boldsymbol{r}_{\beta\alpha}(t) \tag{2.4b}$$

where m_α is the mass of the atom α in the molecule i, $\mu = m_\alpha m_\beta / (m_\alpha + m_\beta)$ is the effective mass, and $\delta \boldsymbol{r}_{\alpha\beta}(t) \equiv \boldsymbol{r}_{i,\alpha}(t) - \boldsymbol{r}_{i,\beta}(t)$. This process is iterated until

$|\delta \boldsymbol{r}^2_{\alpha\beta}(t+\delta t) - d^2_{\alpha\beta}| < \Delta$ for some small tolerance Δ. SHAKE is most effective for large molecules that do not require extremely small tolerances.

2.2.2 Starting the Simulation

Since we wish to study many statepoints extending to low temperature, where relaxation times become large, it is advantageous to use final configurations from higher temperatures as the initial configurations of slightly lower temperatures. This reduces the time it takes to reach equilibrium, which is increasingly important as the temperature is lowered. We considered statepoints of fixed density and temperature. The simulations began with runs at 400 K at each density. When these runs were complete, they provided the initial configurations for the 395 K runs at their respective densities.

To start the 400 K runs, molecules were placed in a cubic lattice with random orientations. Spacing was determined by the given density. Velocities were chosen pseudo-randomly from an interval around the velocity v_T defined by the equipartition theorem equation $3kT = \frac{1}{2}mv^2_T$, with $T = 400$ K, and with the restriction that the net momentum was zero. The cubic lattice configuration results in extremely high potential energy, which is quickly converted to kinetic energy once the simulation begins.

2.2.3 Controlling Temperature

Because the high lattice energy is converted into thermal motion, the temperature of the system increases. In order to keep the temperature at the desired level, it is necessary to scale the velocities. We use the Berendsen "thermal bath" to scale the velocities [37]. This multiplies the velocities by a scale factor χ at every time step. χ is defined

$$\chi = \left[1 + \frac{\delta t}{\tau_T}\left(\frac{T_0}{T} - 1\right)\right]^{\frac{1}{2}}, \tag{2.5}$$

where T_0 is the desired temperature, and τ_T is a time constant that affects the rate of the scaling. It usually takes a value on the order of 1 ps.

2.2.4   Periodic Boundary Conditions

Our simulations used 1728 ($= 12^3$) particles, a relatively large number for water simulations. But even with 1728 particles, if we simulated a closed box, a large fraction (over 33%) of the particles would be "on the surface," and surface effects would be large. To avoid this, the simulation code uses periodic boundary conditions, which create a boundary-less system. The periodic boundary conditions work by having an infinite lattice of identical copies of the original "box" of molecules around a central box. When a molecule moves in the central box, its six corresponding images move in the surrounding boxes. When a molecule goes through the boundary of the central box, it is as if it enters the neighboring box and a new identical particle enters the central box from the opposite side. Since the lattice is periodic, we need only keep track of the molecules in a single simulation cell.

These boundary conditions create a bulk liquid with no surface. Fluctuations that are of large length scale, or correspondingly small reciprocal lattice vectors (on the order of π/L, where L is the length of the side of the box), will therefore be distorted by the finite size. When N is on the order of 100 or greater, such fluctuations do not happen except for state points extremely close to a critical point, therefore this is not an issue in our simulations. Periodic boundary conditions can also affect the rate at which a liquid nucleates, but generally produce accurate results [37].

2.3   Efficient Implementation

2.3.1   Potential Truncation

Done naïvely, determining the potential requires $5N(5N-1)/2$ calculations ($5N$, not N, because there are five sites per molecule and $N(N-1)/2$ is the number of *distinct* pairs), which is $\mathcal{O}(N^2)$ and would make simulation of 1728 particles impractical. However, by truncating the potential at a short-enough cutoff distance r_c, the number of calculations can be reduced to $\mathcal{O}(N)$. The standard practice is

to use a value of r_c around 2.5σ, which is 7.75 Å for ST2. To avoid a discontinuity in the potential, a smooth tapering function $f(r) = 1 - S(r)$ is used.

2.3.2 Correcting the Energy

Truncating the potential will underestimate the potential energy and the virial term of the pressure. The truncation of the Lennard-Jones term is easy to deal with, since it decays with r^{-6} which is convergent. By integrating to ∞, we find the corrections to the potential energy U and pressure P as follows:

$$U_{\text{LJ correction}} = \frac{8\pi\sigma^3 N\epsilon}{3V} \left[\frac{1}{3} \left(\frac{\sigma}{r_c} \right)^9 - \left(\frac{\sigma}{r_c} \right)^3 \right] \simeq .5508\,\text{kJ/mole} \qquad (2.6a)$$

$$P_{\text{LJ correction}} = \frac{16\pi\sigma^3 \epsilon}{3V 62} \left[\frac{2}{3} \left(\frac{\sigma}{r_c} \right)^9 - \left(\frac{\sigma}{r_c} \right)^3 \right] \simeq .3986\,\text{kJ/mole} \qquad (2.6b)$$

The correction to the energy from the Coulomb part of the potential does not converge, since it decays with r^{-1}. There are several methods to correct the pressure and energy, including the Ewald and the fast multipole methods (see [37] for a discussion). We use the computationally efficient reaction field (RF) method due to [47]. The RF method assumes that, for a give point, all molecules more than r_c away are part of a dielectric continuum which is polarized by the dipolar molecules inside the $r < r_c$ sphere. The polarized continuum in turn creates an electric field, called the reaction field $\boldsymbol{\mathcal{E}}_i(r)$, inside the r_c sphere, where i denotes the index of the molecule of interest (located at the center of the sphere). The value of the reaction field at the center of the sphere turns out to be the same as the average value [47], which is.

$$\langle \boldsymbol{\mathcal{E}} \rangle = \frac{1}{\frac{4}{3}\pi r_c^3} \int_0^{r_c} \boldsymbol{\mathcal{E}}(r) d^3 r = \frac{\epsilon - 1}{\epsilon + \frac{1}{2}} \frac{\boldsymbol{M}_i}{r_c^3} \qquad (2.7)$$

where ϵ is the (unknown) dielectric constant of the continuum and $\boldsymbol{M}_i$ is the net dipole moment from the molecules *inside* the $r < r_c$ sphere centered around r_i (all in CGS units) [47, 37].

The dipole moment of the ith molecule is $\boldsymbol{\mu}_i = \sum_{\alpha=1}^4 q_\alpha \boldsymbol{r}_{i,\alpha}$, where α is the

index of the molecular charge q_α. If $\mathcal{S}_i$ is the set of indices $\{j : |r_j - r_i| < r_c\}$, then

$$M_i = \sum_{j \in \boldsymbol{S}_i} \boldsymbol{\mu}_j. \tag{2.8}$$

Since $i \in \mathcal{S}_i$, $\boldsymbol{M}_i$ includes the term $\boldsymbol{\mu}_i \cdot \boldsymbol{\mu}_i = \mu^2$ which is the same for all molecules. For each molecule with dipole moment $\boldsymbol{\mu}_i$, the reaction field contributes $-\frac{1}{2}\boldsymbol{\mu}_i \cdot \langle \boldsymbol{\mathcal{E}}_i \rangle$ to the energy, so the total contribution to the energy is

$$U_{\text{RF}} = -\tfrac{1}{2} \sum_{i=1}^{N} \boldsymbol{\mu}_i \cdot \boldsymbol{\mathcal{E}}_i = -\frac{1}{2}\frac{\epsilon - 1}{\epsilon + \frac{1}{2}} \sum_{i=1}^{N} \sum_{j \in \boldsymbol{S}_i} \frac{\boldsymbol{\mu}_i \cdot \boldsymbol{\mu}_j}{r_c^3} \tag{2.9}$$

We can substitute for the dipole moments to find the energy, first noting that the uncorrected electro-static energy term is

$$U_{\text{electro-static}} = \sum_{i} \sum_{j>i, j \in \mathcal{S}_i} \sum_{\alpha} \sum_{\beta=1}^{4} \frac{q_\alpha q_\beta}{\delta r_{i\alpha,j\beta}} \tag{2.10}$$

where $\delta r_{i\alpha,j\beta} = |\boldsymbol{r}_{i,\alpha} - \boldsymbol{r}_{j,\beta}|$. The $j > i$ ensures that pairs of particles are only counted once. In similar form, the RF correction is given

$$U_{\text{RF}} = \frac{\epsilon - 1}{\epsilon + \frac{1}{2}} \sum_{i} \sum_{j>i, j \in \mathcal{S}_i} \sum_{\alpha} \sum_{\beta=1}^{4} \frac{q_\alpha q_\beta}{r_c^3} (\delta r_{i\alpha,j\beta})^2 - N\frac{1}{2}\frac{\mu^2}{r_c^3} \tag{2.11}$$

where the second term is from the $i = j$ case which is not included in the sum.

There remains the problem that ϵ is unknown, but its actual value is relatively unimportant since the ratio $(\epsilon - 1)/(\epsilon - \frac{1}{2})$ is close to 1 for any reasonable choice of ϵ. In practice, we tacitly assume that $\epsilon = \infty$ and therefore the ratio becomes unity. Hence the total energy due to the electro-static potential and the reaction field (i.e. everything but the Lennard-Jones contribution) is given

$$U_{\text{electro-static total}} = \sum_{i} \sum_{j>i, j \in \mathcal{S}_i} \sum_{\alpha} \sum_{\beta=1}^{4} q_\alpha q_\beta \left[\frac{1}{\delta r_{i\alpha,j\beta}} + \frac{(\delta r_{i\alpha,j\beta})^2}{r_c^3} \right] - N\frac{1}{2}\frac{\mu^2}{r_c^3} \tag{2.12}$$

2.3.3 Neighbor Lists

Though truncating the potential reduces the number of calculations required to find the intermolecular potentials, it introduces a new calculation in order to determine which molecules are within the cutoff r_c. One way of doing this efficiently is to use the Verlet neighbor list [37]. Initially, to every molecule is associated a list of all other molecules within a radius of $r_s \approx 1.05 r_c$, so the list contains at least all the molecules which explicitly contribute to the potential. All lists are recreated whenever the sum of the magnitudes of the two largest molecular displacements is greater than $r_s - r_c$, to ensure that at every time the lists will contain all molecules within the $r < r_c$ sphere. This technique is only an advantage if the lists do not have to be built every time step, so $r_s - r_c$ cannot be too small, but it can also not be too large or else the calculation of the neighbor list (which is $\mathcal{O}(N^2)$) requires too much computation. For this reason, the neighbor list is used in conjunction with linked cell methods for systems of large N.

Chapter 3

Equilibrium Relaxation Behavior

In this chapter, we first cover the expected results for dynamic properties that came out of the analysis. We then explore the unexpected results, focusing primarily on the Stokes-Einstein equation and the Debye-Stokes-Einstein equation.

3.1   Directly Calculated Dynamic Properties

As discussed in Section 1.5, we stored the configurations of molecules $\{\boldsymbol{r}_i\}$ at 100 fs intervals. Equations (1.6), (1.7), (1.18) and (1.19) define $\langle r^2(t) \rangle$, $\langle \phi^2(t) \rangle$, $F_k(t)$, $C_1(t)$ and $C_2(t)$, respectively, in terms of $\{\boldsymbol{r}_i\}$; these quantities are shown in Figures 3.1, 3.2 and 3.3. For statepoints with data spanning more than about 1 ns (i.e. at the lowest temperatures and densities), we only analyzed the data in 1 ps intervals due to RAM constraints. For calculating $F_k(t)$ we had to further limit data to 1 ps intervals whenever we had more than 400 ps of data, and we limited samples to 2 ps intervals in the case of two statepoints that had over 2.5 ns of data. This does not adversely affect the long-time behavior of the functions we will focus on.

Figure 3.1 shows $\langle r^2(t) \rangle$ and $\langle \phi^2(t) \rangle$, over both multiple densities and temperatures. At high temperature, both the mean-squared displacement and the rotational mean-squared displacement show typical ballistic-to-diffuse motion. However, at $T \lesssim 320$ K, both quantities exhibit "plateaus" in between ballistic (char-
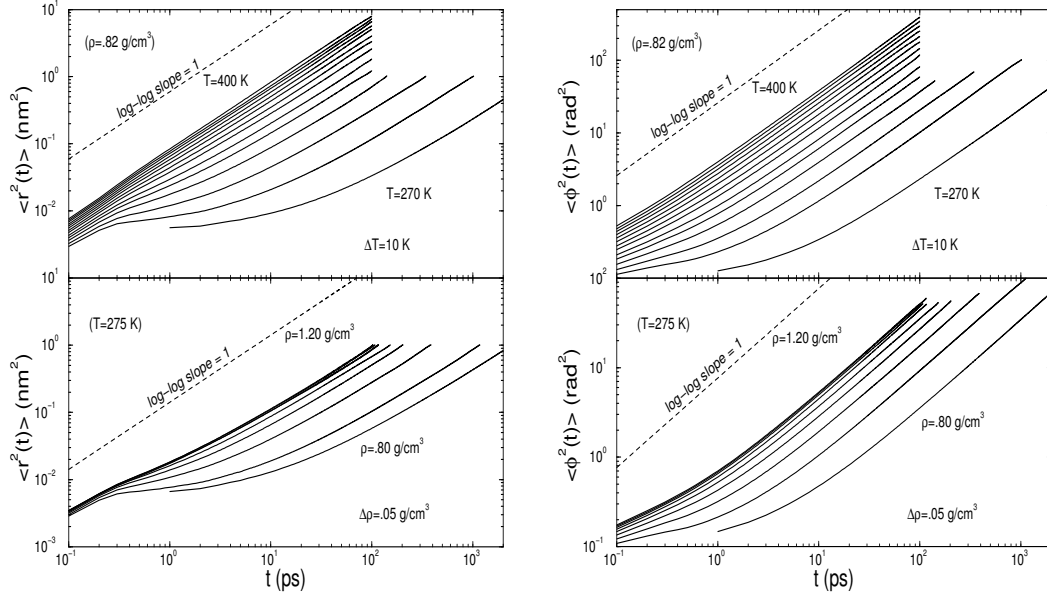
Figure 3.1: Mean Squared Displacement

Mean Squared Displacement $\langle r^2(t)\rangle$ and Rotational Mean Squared Displacement $\langle \phi^2(t)\rangle$, at fixed temperature and fixed density. Not all statepoints are shown for clarity.

acterized by $\langle r^2(t)\rangle \propto t^2$) and diffusive (characterized by $\langle r^2(t)\rangle \propto t$) motion. During this plateau, particles are trapped by their nearest neighbors, and only rattle in a small "cage." In order for the particles to diffuse beyond the size of their cage, their nearest neighbors must move, and for these neighboring particles to move, their neighbors must move as well, etc. This effect is known as caging and becomes increasingly important at lower temperatures. This feedback mechanism is largely responsible for the rapid increase of relaxation time on cooling. The caging effect appears in the mean-squared displacement after about 0.2 ps and can last more than 10 ps, depending on the temperature and density.

Both $\langle r^2(t)\rangle$ and $\langle \phi^2(t)\rangle$ show qualitatively similar dependence on temperature, but differ quantitatively. Referring to Figure 3.1, it is clear that at a fixed density of 0.82 g/cm^3, caging effects appear in $\langle r^2(t)\rangle$ at and below 320 K. At a fixed temperature of 275 K, caging effects appear at all densities abut are most pronounced
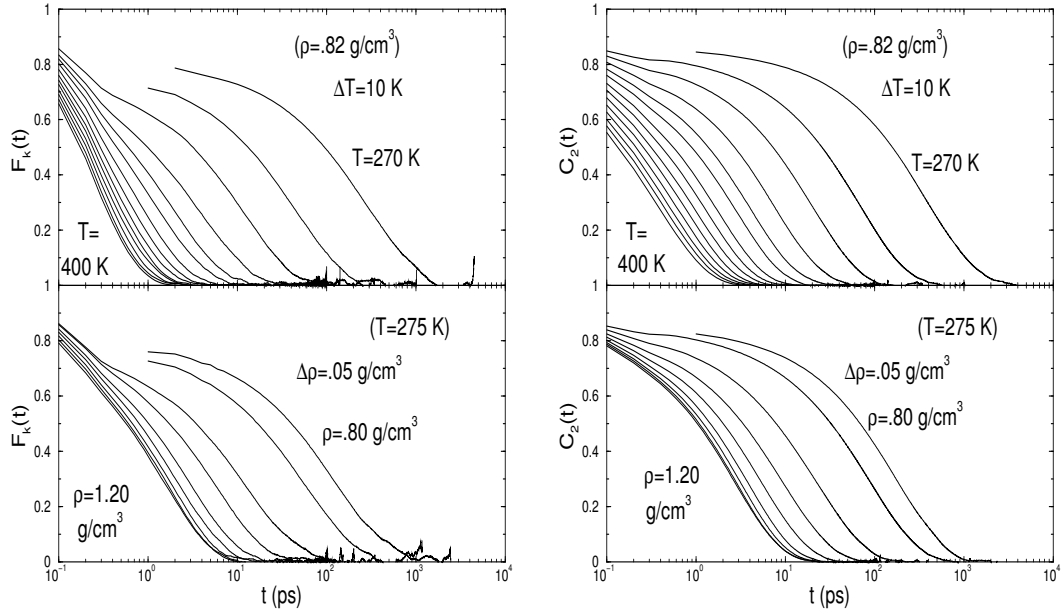
Figure 3.2: $F_k(t)$ and $C_2(t)$

Intermediate scattering function $F_k(t)$ and the 2nd dipole autocorrelation function $C_2(t)$ at fixed temperature and fixed density. Not all statepoints are shown for clarity.

in the lower densities. For $\langle \phi^2(t) \rangle$ at the same fixed density, caging effects are not strong until $T \lesssim 320$ K. At a fixed temperature 275 K, the caging effect in $\langle \phi^2(t) \rangle$ appears in all the isochores and is particularly strong at 0.8 g/cm^3. At the low temperatures and pressures where these caging effects become significant, water is said to exhibit "slow-dynamics". One unresolved question about supercooled water is whether the onset, upon cooling, of translational slow-dynamics occurs at the same temperature of the onset of rotational slow-dynamics. An unambiguous identification of the exact onset temperature is difficult, since the changes with T are gradual. The results from our simulations are inconclusive in this regard, though it is clear that if the translational and rotational onset temperatures differ, they do not do so greatly.

Figure 3.2 shows the temperature and density dependence of $F_k(t)$ and $C_2(t)$. At a fixed density of 0.82 g/cm^3, both quantities show non-exponential behavior

at $T \lesssim 330$ K, which is due to the same caging effect that created the plateau in the mean-squared displacements. $F_k(t)$ measures the correlations over time among all molecules in the simulation, while $C_2(t)$ measures correlations of the angles of the same particle, averaged over all molecules in the simulation. Therefore $F_k(t)$ (and consequently τ_α) is a multi-particle, collective variable, while $C_2(t)$ (and τ_2) is a single-particle variable. The effect of this distinction is hard to see in Figure 3.2 but will become clear later.
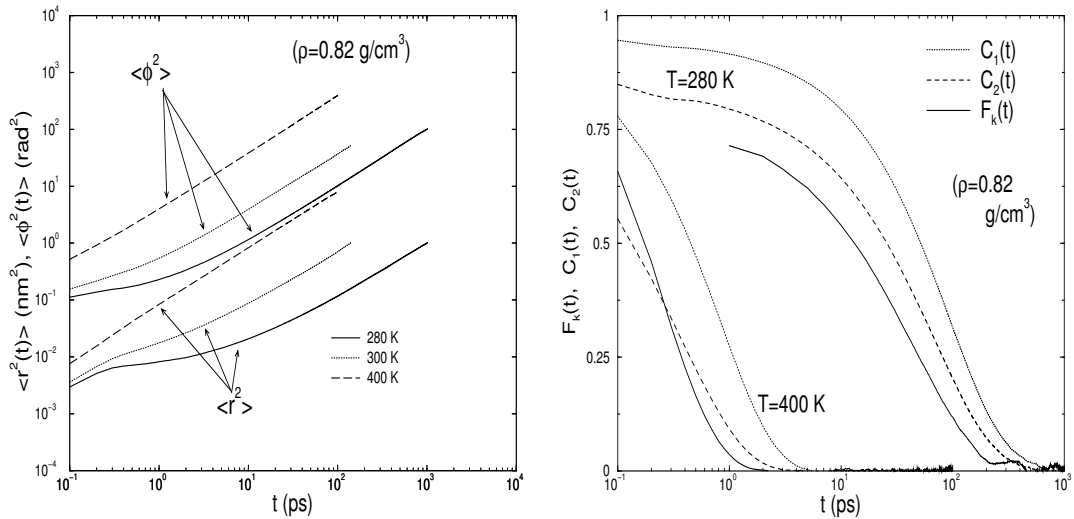
Figure 3.3: Translational quantities compared to rotational quantities (left) $\langle r^2(t) \rangle$ and $\langle \phi^2(t) \rangle$; (right) $F_k(t)$ and $C_1(t)$ and $C_2(t)$.

Figure 3.3 compares $\langle r^2(t) \rangle$ to $\langle \phi^2(t) \rangle$ as well as $F_k(t)$ to $C_l(t)$. At the same statepoint, the translational MSD takes longer to reach the end of the ballistic regime, and hence takes longer to enter the diffusive regime. Thus it can appear that the translational MSD has more caging than the rotational MSD because it takes longer to become diffusive. The effect is due to the different characteristic time scales of translation and rotational and does not imply that caging appears in translational variables and not in rotational variables. Figure 3.4 shows that $\langle r^2(t) \rangle$ and $\langle \phi^2(t) \rangle$ can be scaled in order to nearly match up. It is clear that
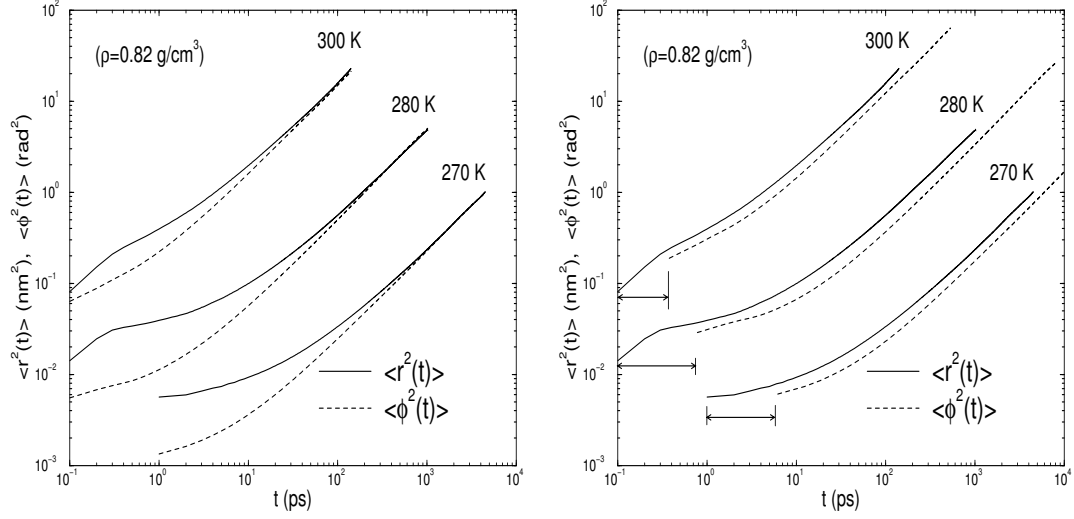
Figure 3.4: $\langle r^2(t) \rangle$ compared to $\langle \phi^2(t) \rangle$

$\langle r^2(t) \rangle$ and $\langle \phi^2(t) \rangle$ in the same plot. $\langle \phi^2(t) \rangle$ shifted vertically in order to facilitate comparison (left), and $\langle \phi^2(t) \rangle$ shifted horizontally (right) to suggest that $\langle \phi^2(t) \rangle$ shows the same behavior as $\langle \phi^2(t) \rangle$ but at earlier temperatures. Because of the log-log scale, values of the shifts are misleading.

$\langle \phi^2(t) \rangle$ consistently becomes diffusive (i.e. a log-log slope of 1) at an earlier time than $\langle r^2(t) \rangle$.

3.2   Time and Diffusion Constants

As mentioned in the introduction, Arrhenius behavior of a quantity Q is characterized by

$$Q \propto e^{E/kT}, \tag{3.1}$$

and hence $\ln(Q) \propto 1/T$, along isobars. If a quantity is Arrhenius, $\ln(Q) \propto 1/T$ generally holds along isochores as well. Figure 3.5 shows time constants and diffusion constants along isobars plotted as natural logarithms as functions of $1/T$. Arrhenius behavior on such plots appears as a straight line. The figure shows cases of non-Arrhenius behavior for the low-pressure isobars of D_{trans}, D_{rot}, τ_α and τ_2. We find markedly non-Arrhenius behavior for $P \lesssim 200$ MPa for all four plots in the figure. The lower the pressure, the greater the effect that cooling has upon slowing the dynamics. The time constants increase more than expected, and the diffusion constants decrease more than expected from the Arrhenius prediction. For $P \gtrsim 200$ MPa, deviations from Arrhenius behavior are small, but are expected to become more pronounced at T lower than we have simulated.

At higher temperatures, the time constants and diffusion constants show little dependence on the pressure, with the exception of D_{trans}. At high temperatures, translational diffusion is greater at low pressures. For $T \lesssim 320$ K, hydrogen bonding becomes significant. High pressures break hydrogen bonds which facilitates diffusion. These effects will be more obvious when we show the behavior along isotherms.

Figure 3.6 shows the same data on isochores and is qualitatively similar to Figure 3.5. The dynamical constants deviate from Arrhenius behavior when $\rho \lesssim 1.05$ g/cm^3. D_{trans} also shows crossover behavior around 320 K. At high temperatures, translational diffusion is greatest at low densities, while at low temperatures, the breaking of hydrogen bonds at high densities becomes non-negligible. Also, as in Figure 3.5, τ_α and τ_2 show extremely similar behavior.

Viewing the time constants and diffusion constants as a function of density along isotherms more clearly demonstrates the effects of the hydrogen bonds. For time constants at low temperatures, the slopes of the isotherms are negative, and
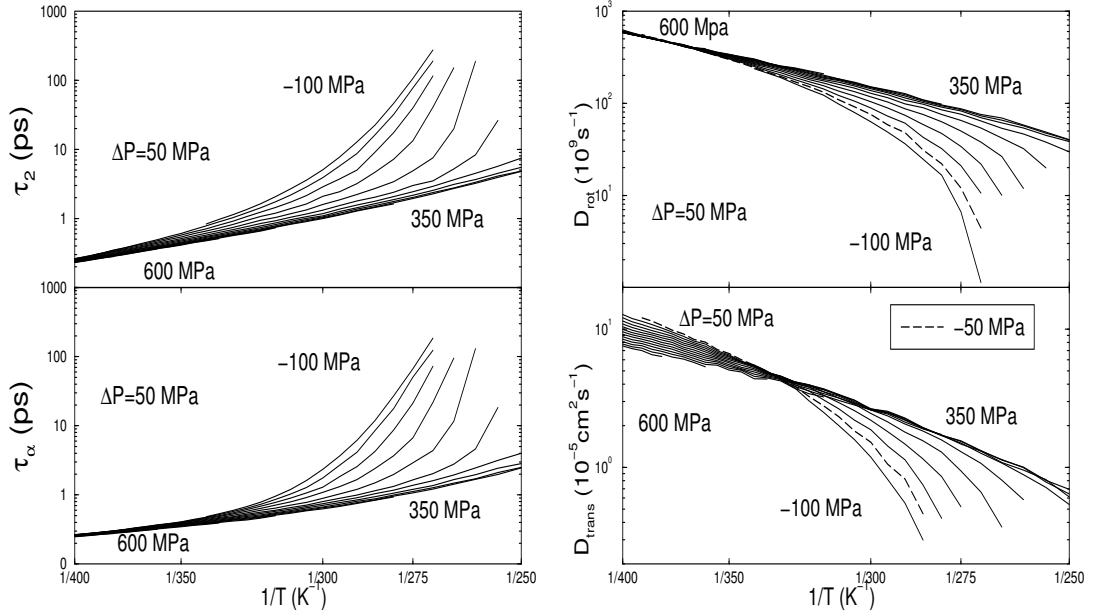
Figure 3.5: Isobars of constants

Isobars of τ_α and τ_2 (left), and of D_{trans} and D_{rot} (right).

the slopes are positive for the diffusion constants at the same low temperatures. This means that as density is increased, molecules are forced out of their preferred tetrahedral structure and consequently the hydrogen bonds are broken. With fewer hydrogen bonds, mobility increases so the diffusion constants increase with pressure and the relaxation times decrease. At even greater pressure, increases in pressure break a smaller fraction of the remaining hydrogen bonds, and mobility decreases due to the packing constraints, and hence the the slopes of τ and D along isotherms change sign. We did not perform simulations at sufficiently high pressure to show this effect. However, we do see that at higher temperatures, there is either little density dependence on the mobility (straight lines) or the intuitive dependence (positive slopes for the time constants and negative slopes for the diffusion constants).

Figure 3.8 shows the dynamical constants along isotherms as a function of pressure, and is similar in form to Figure 3.7, though the change in sign of the slopes between high temperature and low temperature isobars is easier to see. The time
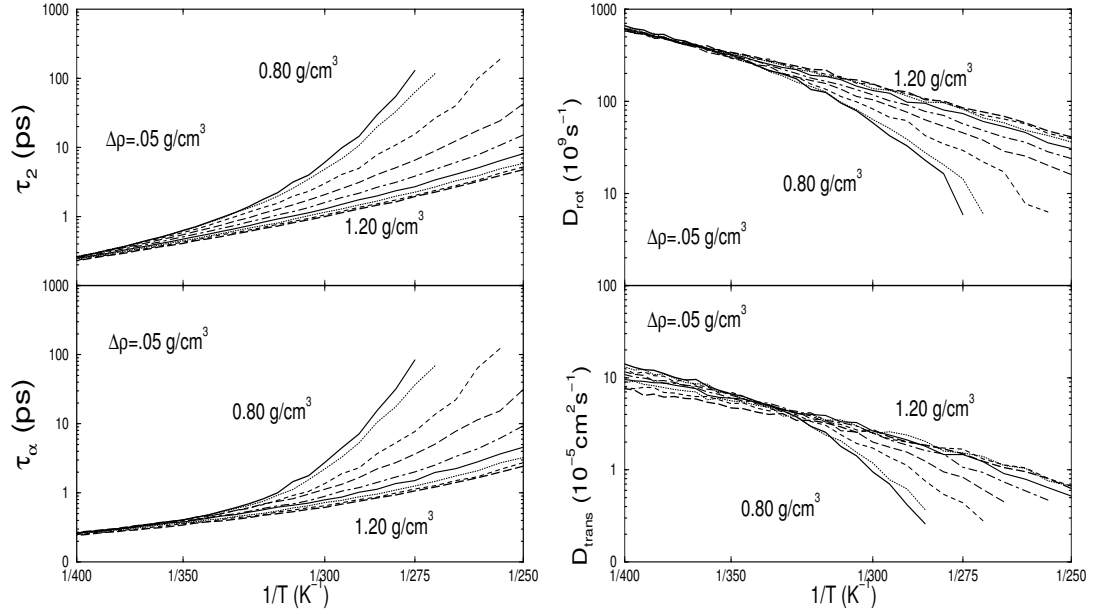
Figure 3.6: Isochores of constants

Isochores of τ_α and τ_2 (left), and of D_{trans} and D_{rot} (right).

constants show the same anomalous behavior, due to breaking hydrogen bonds for $T \lesssim 375$ K, though the effect is not pronounced until $T \lesssim 325$ K. D_{rot} shows the anomalous behavior at $T \lesssim 350$ K, while D_{trans} shows the anomalous behavior at $T \lesssim 330$ K. Because the data are a result from a single simulation at each statepoint, the isotherms are too noisy to determine crossover temperatures with enough certainty to check whether translational and rotational diffusion become anomalous at different temperatures.

The structural relaxation time, τ_α, shows faint but systematic increases in a narrow density range at $\rho \approx 0.91$ g/cm^3 and at $\rho \approx 1.04$ g/cm^3 when viewed isothermally as a function of ρ. As a function of P, these trends appear along curved lines, beginning around 40 MPa and 275 MPa respectively. Figure 3.9 shows these plots in more detail. These trends may be an indication of a critical point, or even two critical points, at lower temperatures. This will be explored further in Chapter 4.
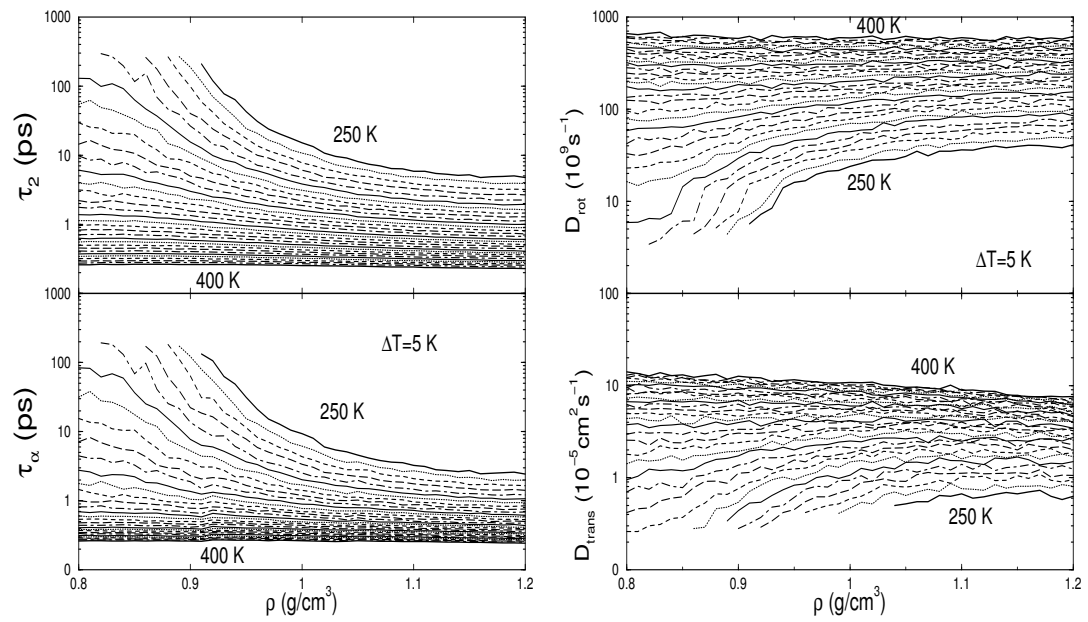
Figure 3.7: Isotherms of constants, as function of ρ

Isotherms of τ_α and τ_2 (left), and of D_{trans} and D_{rot} (right), as a function of density.
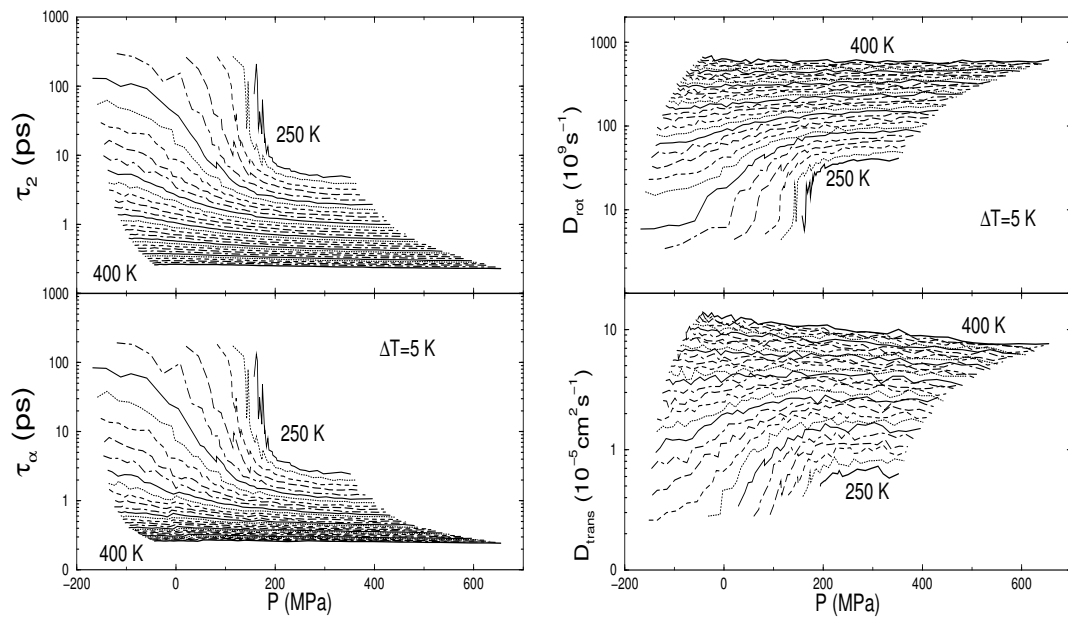
Figure 3.8: Isotherms of constants, as function of P

Isotherms of τ_α and τ_2 (left), and of D_{trans} and D_{rot} (right), as a function of pressure.
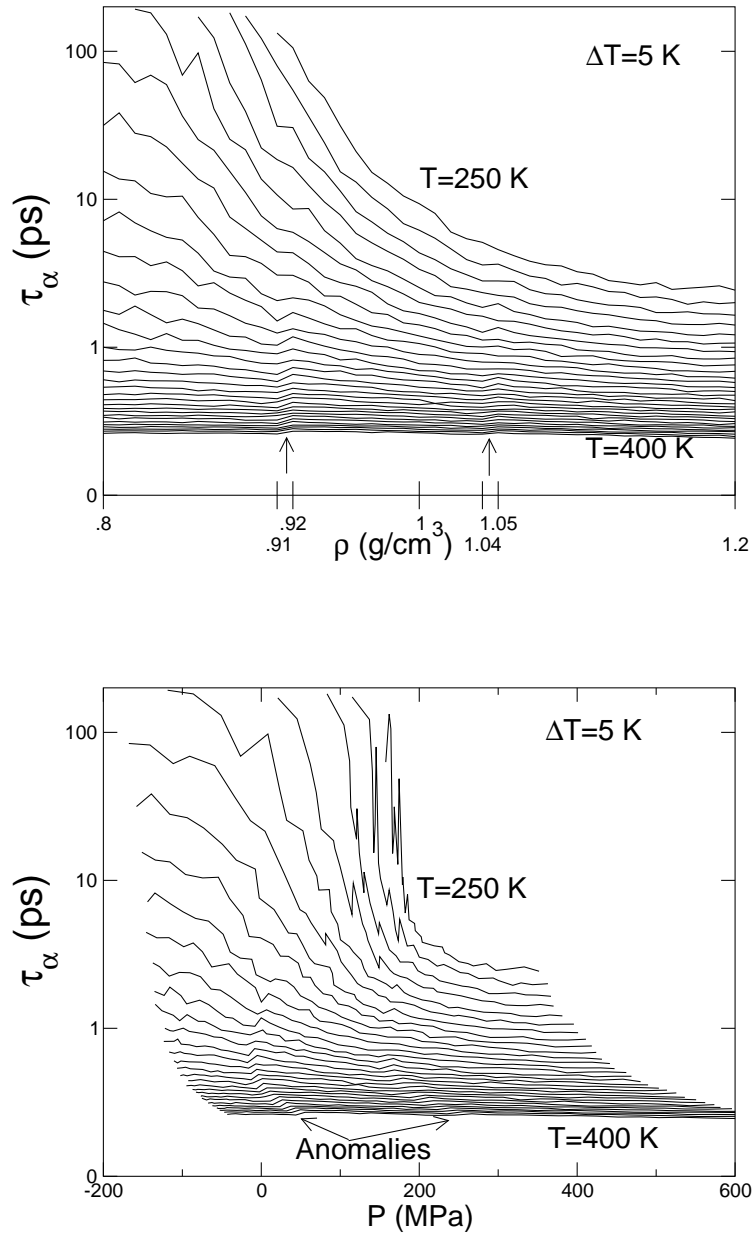
Figure 3.9: Detail of isotherms of τ_α

Isotherms of τ_α as a function of pressure and density, showing the systematic behavior around $\rho = 0.91$ g/cm^3 and around $\rho = 1.04$ g/cm^3.

3.3   Non-Arrhenius Behavior

To characterize a temperature $T_A = T_A(P)$ which marks the change between Arrhenius and non-Arrhenius behavior in τ_α, we can look at plots of

$$kT/E \cdot \ln(\tau/\tau_0), \tag{3.2}$$

where τ_0 is the constant from Equation (1.20). For Arrhenius behavior, this quantity is unity, and thus provides a more sensitive indicator of deviations from Arrhenius behavior. Figure 3.10 (a) shows a graph of $kT/E \cdot \ln(\tau/\tau_0)$, and Figure 3.10 (b) shows a similar graph using τ_2 instead of τ_α. The values $E = E(P)$ and $\tau_0 = \tau_0(P)$ where chosen by least squares best fit of the data at temperatures higher than 375 K, where we expect Arrhenius behavior.
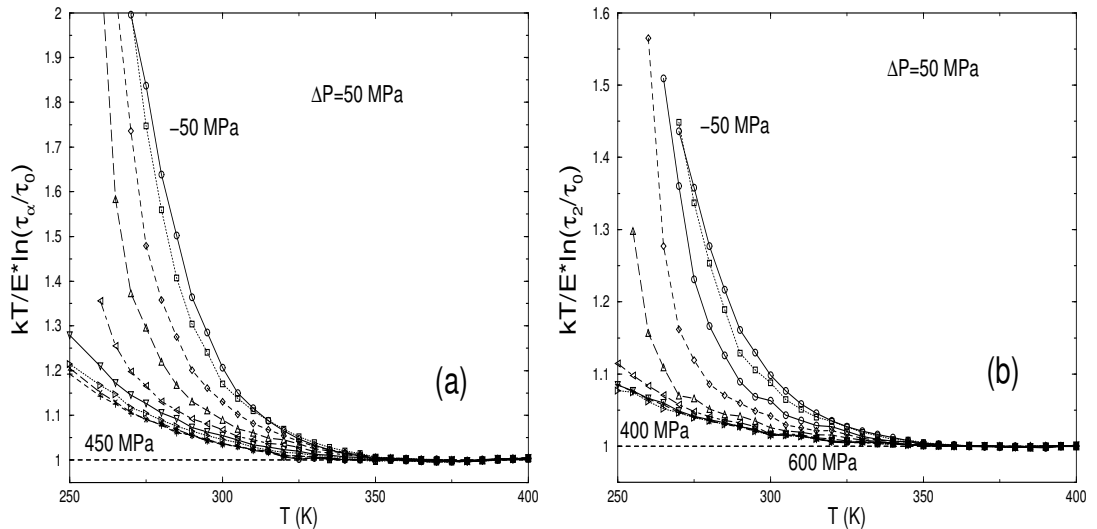
Figure 3.10: Arrhenius plots of τ_α and τ_2

Arrhenius plots of τ_α and τ_2. Arrhenius behavior is indicated by a value of 1.

The figure indicates that both the translational and rotational relaxation times are non-Arrhenius for all pressures, provided that the temperature is low enough. Relaxation times deviate more from Arrhenius behavior at lower pressure.
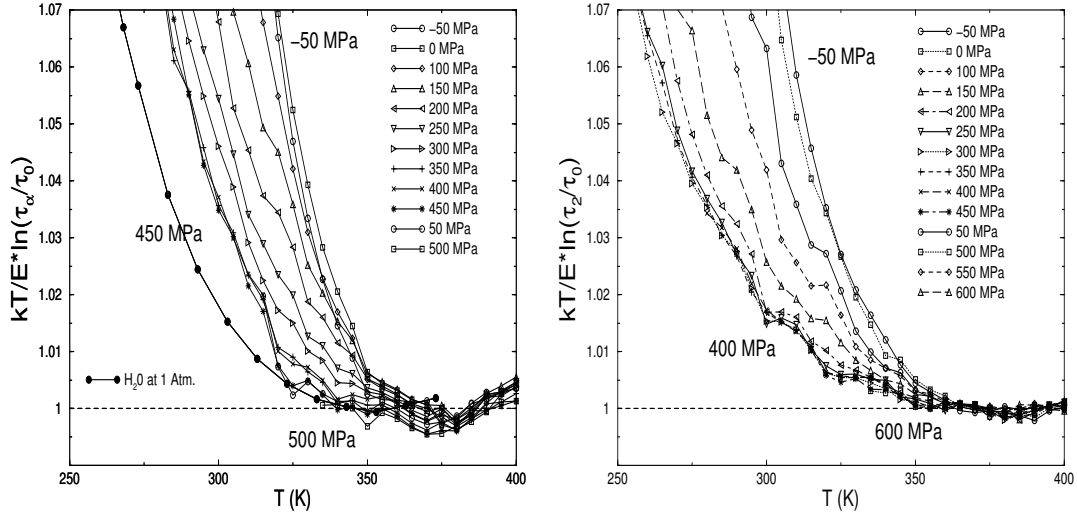
Figure 3.11: Detail of Figure 3.10

Arrhenius plots of τ_α and τ_2, similar to Figure 3.10 but in more detail on the vertical axis. Dark circles are data for real water, from [33].

Figure 3.11 shows the same quantities as Figure 3.10 but in more detail on the vertical axis, showing that at high temperatures, the time constants are very nearly Arrhenius. The deviations in this upper region are tiny, and make it easier to determine a temperature T_A when the behavior is no longer Arrhenius. This figure was used to crudely estimate the T_A for rotation and translation, and T_A is shown in Figure 3.25. The values of T_A and $T_{A,rot}$ are not identical, but the difference is comparable to the error in determining T_A. The error bars shown in Figure 3.25 reflect possible error in finding T_A given Figure 3.11, and do not take into account error from using single simulations at each statepoint nor error from calculating $E(P)$ and $\tau_0(P)$ from the $T > 275$ K data.

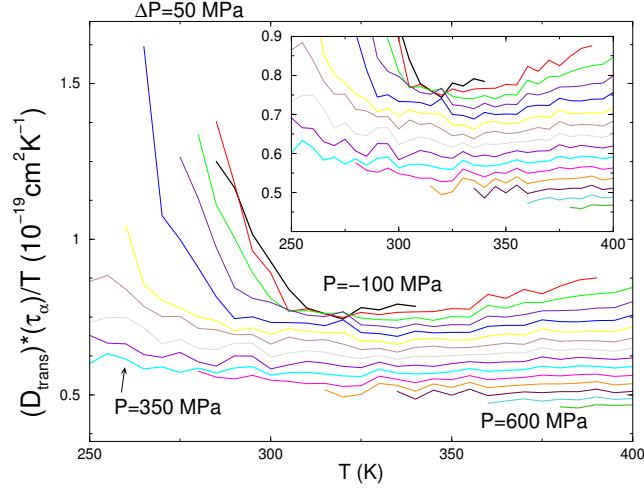## 3.4 Breakdown of Stokes-Einstein

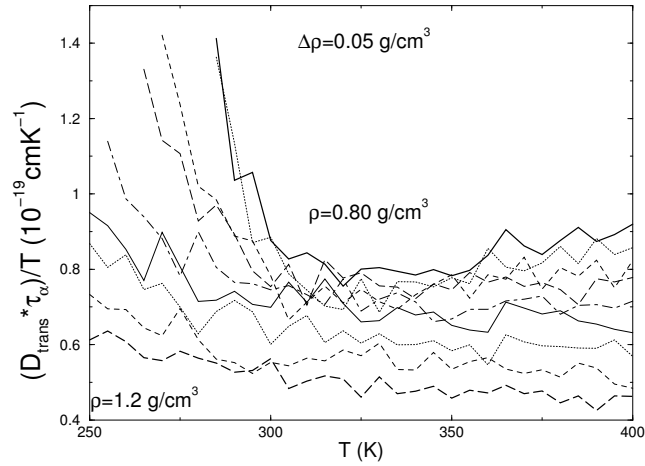Figure 3.12: $(D_{trans}\tau_\alpha)/T$ along isobars

$(D_{trans}\tau_\alpha)/T$ is non-constant at low temperatures, indicating that the Stokes-Einstein Equation is no longer valid

Figure 3.12 plots $D_{trans}\tau_\alpha/T$ along isobars in order to test the Stokes-Einstein equation (1.11); that is, we test if $D_{trans}\eta/T$ is a constant. Because we have not calculated η, we use τ_α, since fluid dynamics predicts that

$$\eta = G_\infty \tau_\alpha, \tag{3.3}$$

where G_∞ is the infinite frequency shear modulus and is nearly T-independent [30]. Hence our results should not be strongly affected by using τ_α. To follow up on this point, we plan to confirm that $\tau_\alpha \propto \eta$, or use η directly should the proportionality fail for our simulations of water. For the present work, we did not calculate η because it requires data on velocity, which were not stored during data runs.

As the Figure 3.12 shows, $D_{trans}\tau_\alpha/T$ along isobars increases dramatically for $T \lesssim 310$ K. We have subjectively assigned a breakdown temperature $T_{SE} = T_{SE}(P)$ to each isobar which marks the lowest temperature of good agreement with the SE equation (figure 3.25). Because the $D_{trans}\tau_\alpha/T$ increases, this means D_{trans}

Figure 3.13: $(D_{trans}\tau_\alpha)/T$ along isochores
Similar to Figure 3.12 but along isochores. Top plot is linear-log scale, buttom plot is linear-linear scale in detail.

does not decay as quickly as $1/\tau_\alpha$; this phenomena has been called "enhanced translational diffusion" in the literature, and has meaning only in the sense that D_{trans} is enhanced relative to $1/\tau_\alpha$. Note that $D_{trans}\tau_\alpha/T$ is not constant along isochores either; see Figure 3.13.

Reference [40] provides a simple argument to explain the breakdown of Stokes-Einstein and the enhancement of translational diffusion (in comparison to a time constant). The following argument is *not* specific to D_{trans} and can be applied to D_{rot} as well, a fact that has not been appreciated in previous work; this will be important in the next section. Similarly, we use τ to mean either τ_α or τ_2. As we cool below the onset of non-Arrhenius behavior temperature dependence, the dynamics of water (and other liquids) is known to become increasingly spatially heterogeneous [38, 39]. Assume that a fraction α of the molecules are in local regions of mobility greater than average ("fast regions"), and a fraction $(1-\alpha)$ are in regions of diminished mobility ("slow regions"). Further, we assume that the SE equation holds locally in the fast and slow regions. We can write the
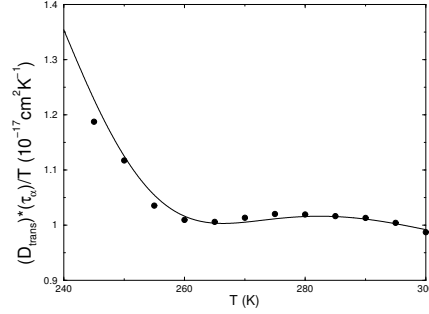
Figure 3.14: Stokes-Einstein for Water

$(D_{trans}\tau_\alpha)/T$ along isobars using data on water from [33], showing that the behavior for ST2 is qualitatively similar to that of real water

overall diffusion constant and the the relaxation time as

$$D = \alpha D_{fast} + (1 - \alpha)D_{slow} \tag{3.4a}$$

$$\tau = \alpha \tau_{fast} + (1 - \alpha)\tau_{slow}. \tag{3.4b}$$

If α is not too small and the degree of heterogeneity is significant, meaning that $D_{fast} \gg D_{slow}$ and $\tau_{fast} \ll \tau_{slow}$, then

$$D \approx \alpha D_{fast} \tag{3.5a}$$

$$\tau \approx (1 - \alpha)\tau_{slow}. \tag{3.5b}$$

In other words, D is dominated by fast regions, while τ is dominated by slow regions. Because the SE equation holds locally, we have $D_{fast}\tau_{fast}/T$ and $D_{slow}\tau_{slow}/T$ are constant. Since $D_{fast} \neq D_{slow}$, then $D_{fast}\tau_{slow}/T > D_{slow}\tau_{slow}/T$ and hence is non-constant. In the approximation of Equation (3.5b), this implies that $D\tau/T$ is not constant and that diffusion is "enhanced."

There is strong evidence that water is indeed heterogeneous at low temperatures [38, 39]. However, the above interpretation makes oversimplified assumptions about the nature of the heterogeneities.

Experimental evidence has shown that the SE equation breaks down in other fragile glass-forming liquids. Since 1990, studies on *o*-terphenyl (OTP) have tracked viscosity for up to 14 decades and found enhanced translational diffusion [40, 48, 49, 50, 51, 52, 53, 54, 55]. OTP is frequently studied because it does not easily crystallize and hence is an excellent glass forming liquid. Refs. [48] and [55] suggested that a fractional Stokes-Einstein equation

$$D_{trans} \propto \frac{T}{\eta^\epsilon}, \quad \epsilon < 1 \tag{3.6}$$

may be appropriate at lower T. SE has also been found to break down in the fragile glass former 1,3-bis-(1-naphthyl)-5-(2-naphthyl)benzene ($\alpha\alpha\beta$-TNB) [56, 55]. Recent computer simulations of binary Lennard-Jones liquids [57] and fragile glass formers [58] have also found the SE equation to fail at low temperatures. References [39, 38] provide a good review of previous work.

3.5   Breakdown of Debye-Stokes-Einstein

As mentioned in the previous section, it seems that the argument for enhanced translational diffusion can be applied for rotational diffusion as well, predicting that D_{rot} is enhanced, relative to either τ_α or τ_2. However, this enhancement has not been found in previous literature. Studies on OTP [48, 49, 54, 40] and on $\alpha\alpha\beta$-TNB [56] using τ_2^{-1} in place of D_{rot} have found the DSE equation to hold to $T < 1.2T_g$. The assumption that $D_{rot} \propto \tau_2^{-1}$ is sometimes tacitly assumed in these experimental papers, since D_{rot} is not an easily accessible experimental quantity. As a result, there has been an idea of a "translational-rotational" paradox [39, 38, 53] since, as previously mentioned, it was found that D_{trans} is enhanced at low T. One suggested explanation for this paradox [38, 39] is a heterogeneity theory called the "fluidized domain" model. It argues that in fast regions ("fluidized" regions), which exist over a time scale t_0, rotational diffusion is enhanced only when the domain is first created in an "un-locking" process. The translational diffusion is enhanced during the entire interval t_0 until the region vanishes, as molecules reorder into lower-energy structured regions. As a result, the translational diffusion is enhanced more strongly than rotational diffusion.

With computer simulations, we have the luxury of being able to calculate both D_{rot} and τ_2, so we can check the assumption that $D_{rot} \propto \tau_2^{-1}$. As T decreases, diffusion slows down so D_{rot} decreases and the time required for the system to relax (whether rotationally or translationally) increases, hence $1/\tau_2$ decreases as well. The assumption has also been made out of necessity, since experiments cannot measure D_{rot}.

The same reasoning that argued for an enhancement of D_{trans} with respect to τ_α applies to any D and τ, and hence that reasoning would suggest that $D_{rot}\tau_2$ is not constant. Our results support this reasoning. Figure 3.15 shows the value of $\tau_2 D_{rot}$ along isobars as a function of temperature. At most temperature and pressures, the slope on the isobar is negative, meaning that D_{rot} is enhanced compared to $1/\tau_2$, and hence that the assumption of proportionality breaks down. The change in slope at low temperatures in the lowest pressure isobars is not well
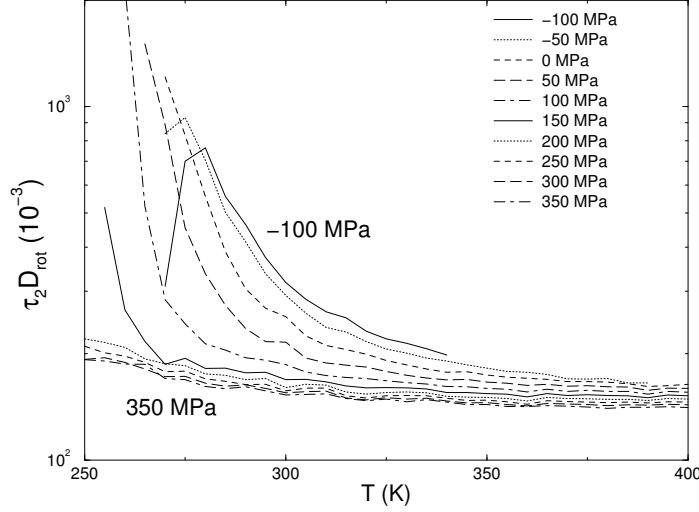
Figure 3.15: $D_{rot}\tau_2$ along isobars

$D_{rot}\tau_2$, shown along isobars. The assumption that $D_{rot} \propto 1/\tau_2$ is not a good one at low temperatures. The change in slope on the -50 MPA and -100 MPa isobars may be due to noise, since the value of D_{rot} is extremely low and the value of τ_2 is extremely high. See Figure 3.16.

understood (Figure 3.16). This change in slope means that D_{rot} is decreasing with temperature faster than $1/\tau_2$ decreases. Figure 3.17 confirms that the same behavior occurs along isochoric paths. A simple explanation of this may be that as the liquid is cooled, it forms many strong tetrahedral bonds – though without long range order – and fewer and fewer patches of fast-moving heterogeneities appear. In terms of eq. (3.4a), this means $\alpha \to 0$ and $(1 - \alpha) \to 1$. Because time constants are dominated by slow regions, they continue to be dominated by slow regions as the whole liquid becomes nearly uniformly slow. The diffusion constants, however, are dominated by fast regions, but as the proportion of liquid in a fast-moving region goes to 0, the diffusion constants are necessarily dominated by the slow-moving regions, and hence the "enhanced diffusion" that occurs at moderately low temperatures ceases to exist, explaining the relative decline in
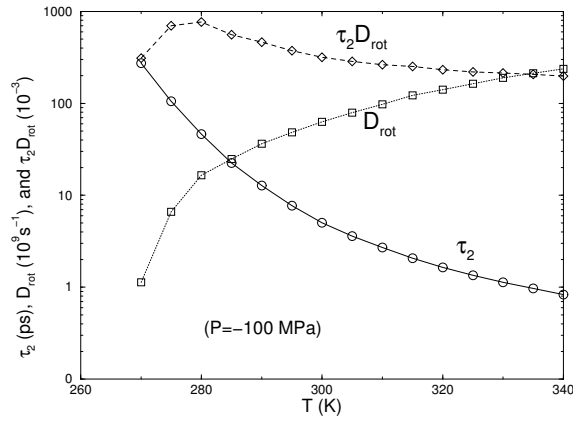
Figure 3.16: $D_{rot}\tau_2$ along isobars, log scale

D_{rot}, τ_2, and $\tau_2 D_{rot}$ shown along isobars on a linear-log scale. The extreme values of the relaxation and diffusion constants at low temperatures introduce large uncertainties into the product, which may explains the change in slope at very low temperatures. If the change of slope is physical, its cause remains unexplained.
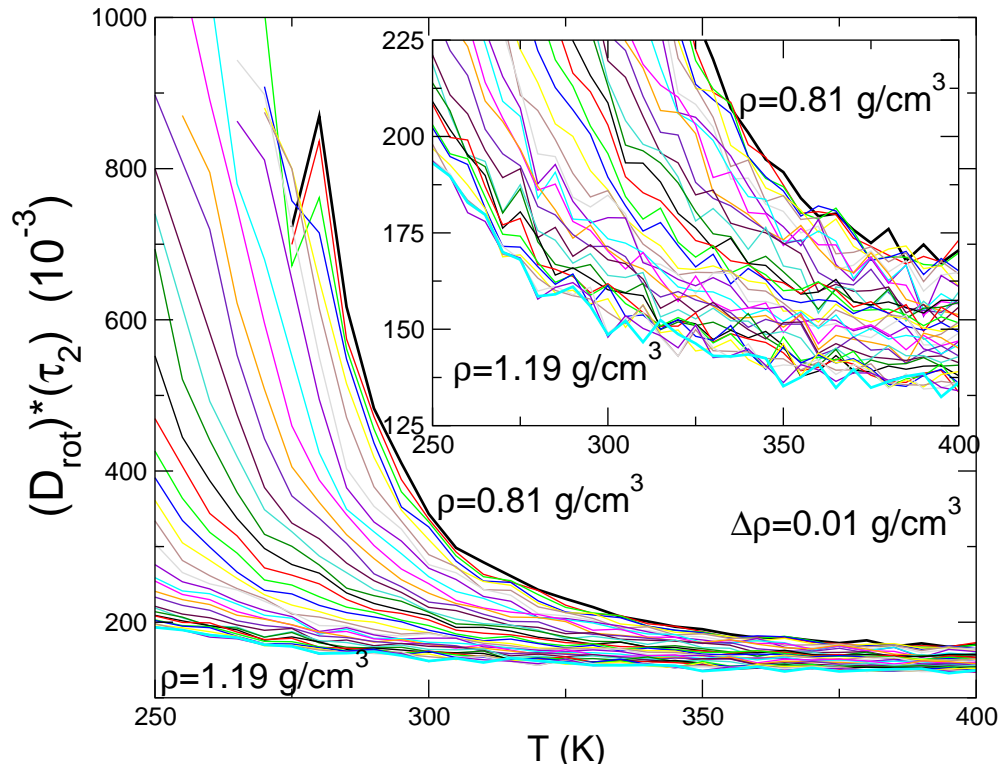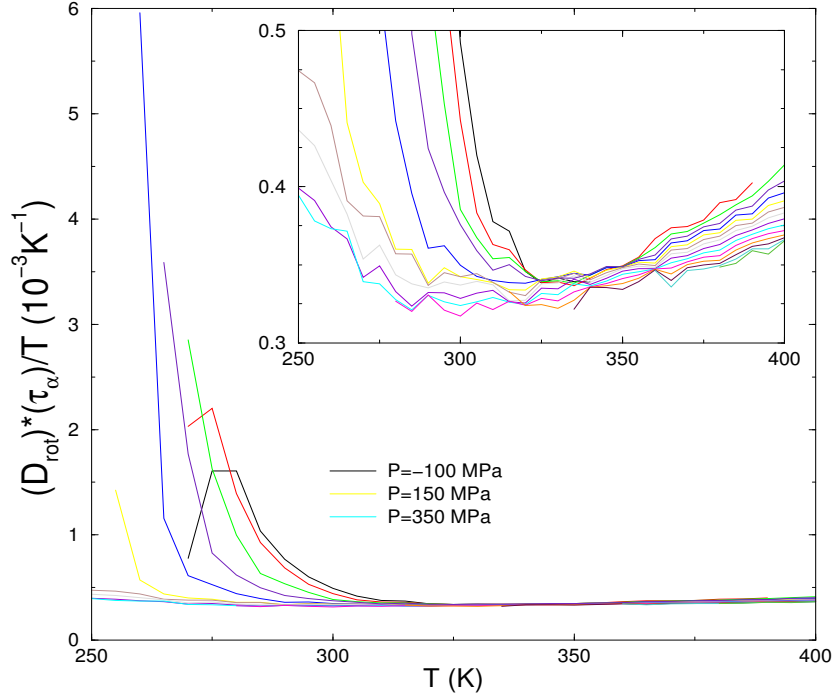
D_{rot}.

Figure 3.17: $\tau_2 D_{rot}$ along isochores

$\tau_2 D_{rot}$, shown along isochores. The isochoric behavior is qualitatively similar to the isobaric behavior; see Figure 3.15. Each shown isochore at ρ_0 is actually the average of the three isochores $\rho_0 - .01$, ρ_0 and $\rho_0 + .01$ g/cm^3.

Figure 3.18: $(D_{rot}\tau_\alpha)/T$ along isobars

$(D_{rot}\tau_\alpha)/T$ is predicted to be constant along isobars by the DSE equation. At low temperatures, $(D_{rot}\tau_\alpha)/T$ is clearly not constant. The inset is zoomed in on the x-axis.

Since $D_{rot} \not\propto \tau_2^{-1}$, this calls into question the validity of results claiming that the DSE equation (eq. 1.12) holds at low T. Hence, we plot $(D_{rot}\tau_\alpha)/T$ along isobars (Figure 3.18) and isochores (Figure 3.19) as well as $(\tau_2^{-1}\tau_\alpha)/T$ along isobars (Figure 3.20). We show both D_{rot} and τ_2^{-1} because our results show that the two quantities are not coupled at low temperatures. At low temperatures, the quantity $(D_{rot}\tau_\alpha)/T$ increases along isobaric or isochoric paths, meaning that D_{rot} is enhanced in comparison to $1/\tau_\alpha$ and that the DSE equation does not hold. The quantity $(\tau_2^{-1}\tau_\alpha)/T$ also initially increases at low temperatures when plotted along isobars (Figure 3.20); the behavior of $(\tau_2^{-1}\tau_\alpha)/T$ along isochores is particularly interesting and is the topic of the next chapter. Thus, our data suggest that
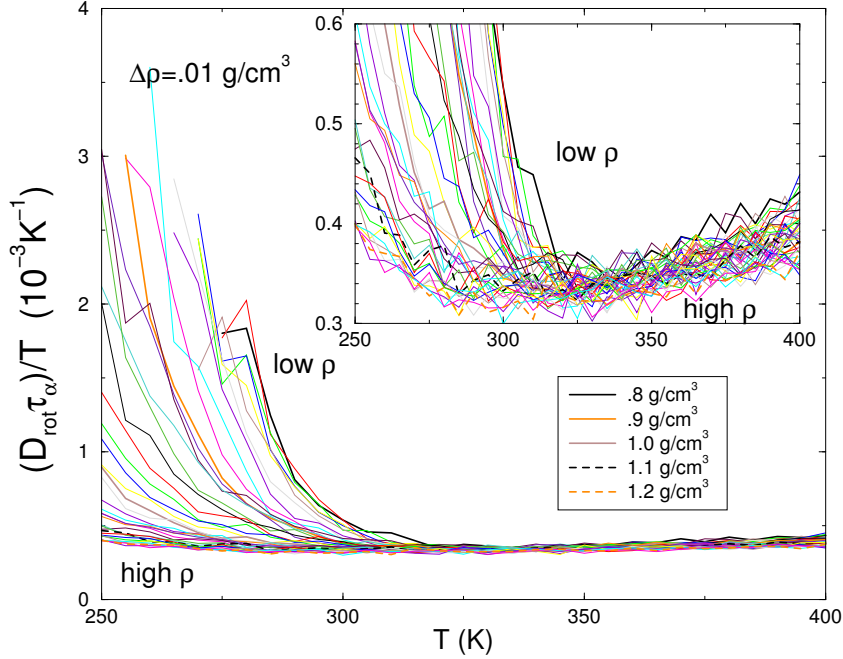
Figure 3.19: $(D_{rot}\tau_\alpha)/T$ along isochores

Similar to Figure 3.18 but along isochores. The inset is zoomed in on the x-axis.

the Debye-Stokes-Einstein does not hold at low-temperature, in analogy to the failure of the Stokes-Einstein equation, and in contrast with results from most other fragile glass forming liquids.

There have been a few papers supporting the idea that the DSE equation does not hold at low temperatures in experiments on $\alpha\alpha\beta$-TNB [50], OTP [59, 60], and on computer simulation of rigid Lennard-Jones dumbells [61]. As noted previously, other studies on OTP and $\alpha\alpha\beta$-TNB have found the DSE to hold. It is not clear why there have been conflicting results. The weak but ubiquitous assumption that $D_{rot} \propto \tau_2^{-1}$ further complicates analysis. It may also be that OTP and $\alpha\alpha\beta$-TNB show behavior different than water because they are non-associative liquids (since they do not form a network of bonds). The argument put forward to explain
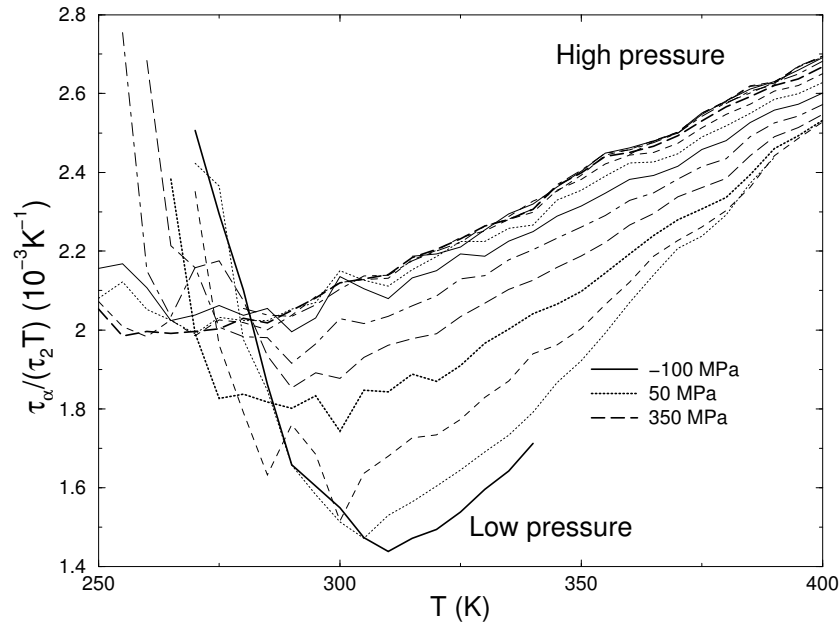
Figure 3.20: DSE using $1/\tau_2$

Testing Debye-Stokes-Einstein with $1/\tau_2$, as previous literature has done, instead of using D_{rot}. Note that DSE does *not* hold even using $1/\tau_2$, in contrast to many experimental results.

enhancement of D relative to τ is overly simple, and a complete explanation of the breakdown in the DSE equation is currently lacking.

3.6   Enhancement of Rotational Diffusion

If both the SE and DSE equations hold, then necessarily we have than $D_{trans} \propto D_{rot}$, since both are proportional to $T/\eta, (\propto T/\tau_\alpha)$. Figures (3.12 - 3.20) show that this is not the case; moreover, these figures show an enhancement of both D_{trans} and D_{rot} relative to τ_α. We next consider the *relative* enhancement of these quantities. If both the SE and DSE equations fail in the same way (i.e. replaced by

$$D \propto \frac{T}{\eta^\epsilon} \tag{3.7}$$

for some $\epsilon < 1$), then we would still expect $D_{trans} \propto D_{rot}$. However, we find that this is not the case, since at low temperatures, the ratio D_{rot}/D_{trans} is not constant (Figure 3.21).
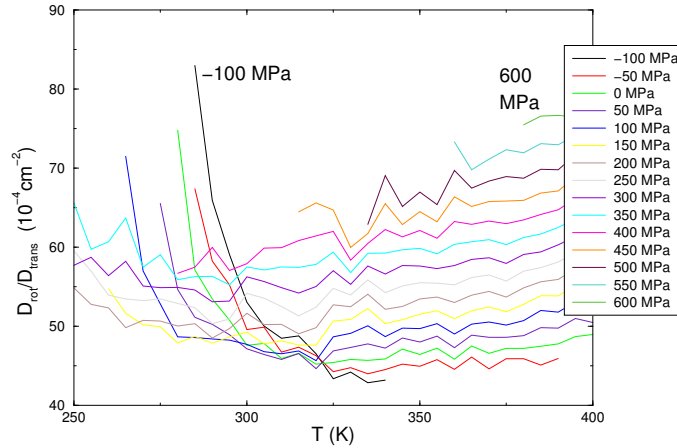

Figure 3.21: D_{rot}/D_{trans} along isobars

D_{rot}/D_{trans} along isobars as a function of temperature. The ratio is not constant at low temperatures. Along isochores, the trend is similar, though the data are prohibitively noisy to plot.
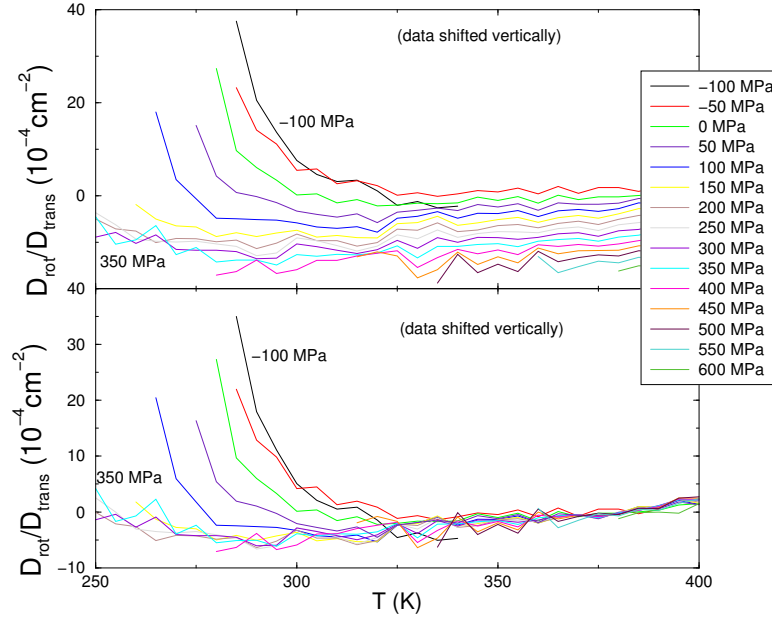
Figure 3.22: D_{rot}/D_{trans} along isobars, shifted vertically

D_{rot}/D_{trans} along isobars as a function of temperature. These are the same quantities as in Figure 3.21 but the isobars have been shifted vertically for clarity. In the bottom plot, the isobars have been shifted so that the average of the final ten data points is 0, while the isobars in the top plot have been additionally shifted by a value of -2.5 per 100 MPa.

Fig. 3.21 demonstrates that D_{rot} is enhanced relative to D_{trans}, but the data are too noisy to define a clear crossover temperature that marks the end of proportionality. Figure 3.22 shows the same ratio but with shifted isobars to increase the transparency. Though not shown, there is similar behavior along isochores with even more noise and a less pronounced increase in D_{rot}. If $1/\tau_2 \propto D_{rot}$, then we would expect $(D_{trans}\tau_2)^{-1}$ to be similar to Figure 3.21. This is not the case, for in Figure 3.23 the data go negative at low temperatures, implying that $D_{rot} > 1/\tau_2$, and hence $D_{rot}\tau_2 > 1$, which is indeed what Figure 3.15 shows. Figures 3.21 and 3.22 show that upon cooling, rotational diffusive motion does not slow down as much as the translational motion does. This is the opposite of previous claims of
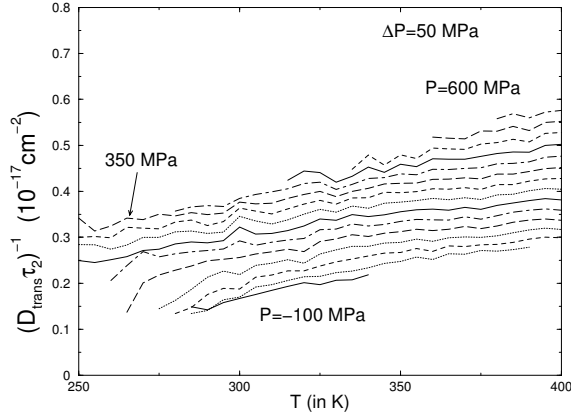
Figure 3.23: $(D_{trans}\tau_2)^{-1}$ along isobars

$(D_{trans}\tau_2)^{-1}$ along isobars as a function of temperature.

enhanced diffusion [39, 53, 54]. However, there have been NMR studies measuring the spin-lattice relaxation time of protons in water that find at low temperature, the relaxation rate T_1 is dominated by the intramolecular relaxation rate, as opposed to the intermolecular relaxation rate [62, 63]. Because the intramolecular relaxation rate (which is a rate, so proportional to τ_2^{-1}) is only affected by rotations – while the intermolecular relaxation rate is affected by translations as well – this means that rotational diffusion is larger than translational diffusion at low temperatures, in agreement with our observations.

It is tempting to find a simple explanation using heterogeneities; one could argue, for example, that in clusters of mobile atoms, translational diffusion is limited by the size of the cluster, while there is no similar constraint on rotation. However, these simple arguments are easy to turn into contradictions, and it was arguments such as these that originally led to the questionable idea of "enhanced *translational* diffusion." At the present time, we defer an explanation of the underlying mechanism behind the increase in rotational mobility to a future published version of this work. It may be that a theory describing the mechanisms
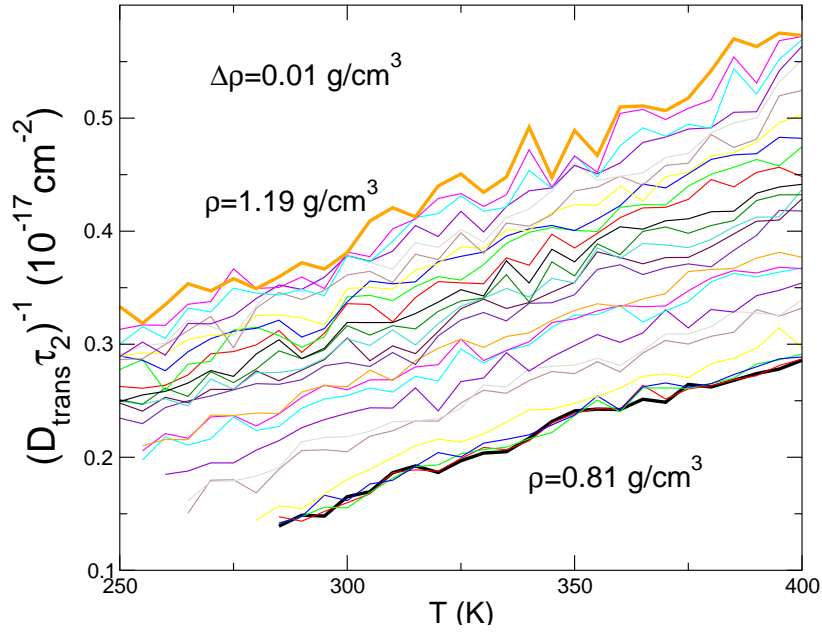
Figure 3.24: $(D_{trans}\tau_2)^{-1}$ along isochores

$(D_{trans}\tau_2)^{-1}$ along isochores as a function of temperature. The behavior along isochores is very similar to that along isobars; see Figure 3.23. Each shown isochore at ρ_0 is actually the average of the three isochores $\rho_0 - .01$, ρ_0 and $\rho_0 + .01$ g/cm^3.

that allows liquids to diffuse faster than expected by the SE and DSE equations will explain why rotational diffusion decreases less rapidly with decreasing T than translational diffusion.

3.7 Summary of Characteristic Temperatures

In this chapter, we have quantified the temperatures of the breakdown of Arrhenius behavior, the SE equation and the DSE equation. To put these results in context, we show loci of these breakdown temperatures in Figure 3.25. The breakdown of Arrhenius behavior of both rotational and translational relaxation occurs $\approx$30-40 K above the melting temperature T_m, nearly independent of pressure. For comparison, the data for water at 1 Atm. show the breakdown occurs $\approx$50 K above T_m (Figure 3.11). The measures of the breakdown of the SE and DSE equations occur at $\approx$0-20 K below T_m, weakly dependent on P. For water at 1 Atm., the breakdown occurs at $\approx$15 K below T_m. Hence our results are largely comparable to real water, and we are able to probe a wider range of T and P than can be easily experimentally accessed.
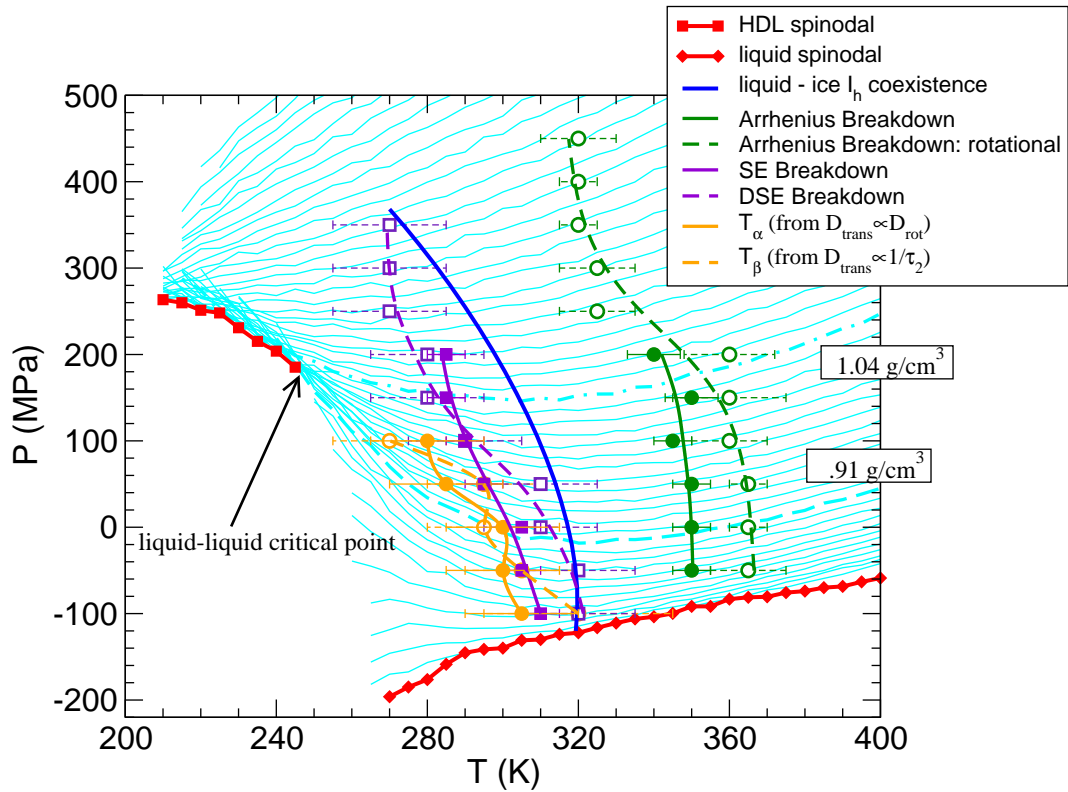
Figure 3.25: Computationally determined PT diagram for ST2

The computationally determined phase diagram for ST water, showing the roughly estimated lines T_α and T_β, which correspond to the breakdown of D_{rot}/D_{trans} and $(D_{trans}\tau_2)^{-1}$ respectively, as well as estimated lines for the breakdown of the SE and DSE equations and the breakdown of Arrhenius behavior in translational and rotational dynamics. All other data from P. H. Poole (private communication).

Chapter 4

Dynamic Precursor to Phase Separation

The most unexpected result that came of the data is a possible precursor to liquid-liquid phase separation, found in even the highest temperatures simulated (400 K). There may also be evidence of a precursor to a second liquid-liquid phase transition at $\rho \approx 1.04$ g/cm^3. Such precursors have not previously been seen at such high temperatures, and were only noticeable in the present data because of the exceptionally fine spacing of the isochores.

To test the Debye-Stokes-Einstein relation, we plotted $D_{rot}\tau_\alpha/T$ along isobars, and in Figure 3.20 we plotted $\tau_\alpha/(T\tau_2)$ to see if the DSE equation would hold if we used the approximation $D_{rot} \propto 1/\tau_2$ as done in many experiments. Because our runs were carried out along isochoric paths, isobaric data was created by extrapolating values from splined curves of isotherms as a function of pressure. We chose to space isobars at 50 MPa intervals over the range -100 MPa to 600 MPa, though only the 0 MPa to 350 MPa isobars contained data on the full range of temperatures, giving seven complete isobars. In contrast to this coarse spacing, the isochoric data was spaced in .01 g/cm^3 intervals over the range 0.80 g/cm^3 to 1.20 g/cm^3, giving 41 isochores, with 30 isochores containing data on the full range of temperatures.

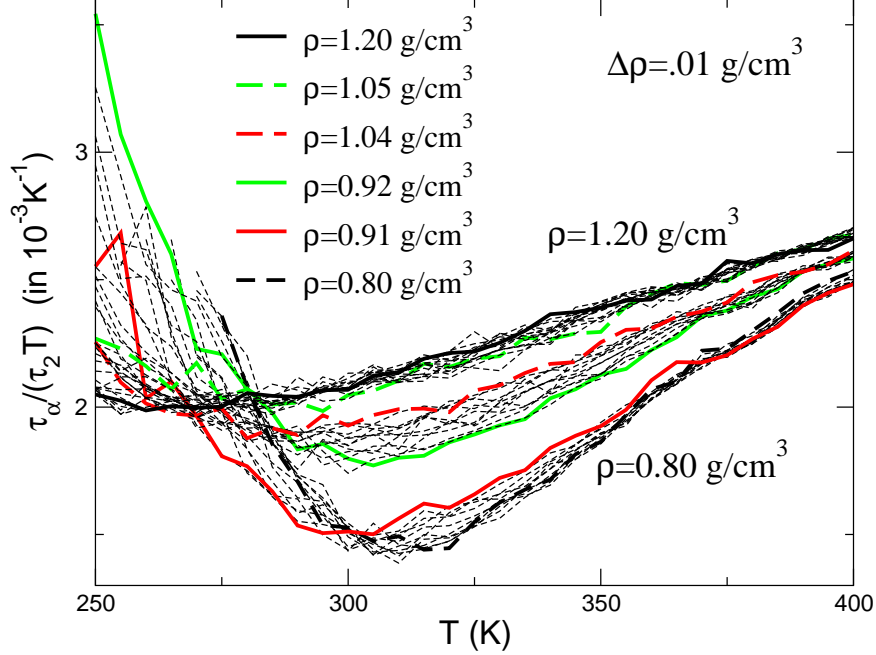Figure 4.1 shows the same quantity as Figure 3.20, $\tau_\alpha/(T\tau_2)$, but along iso-

Figure 4.1: Isochores of $\tau_\alpha/(T\tau_2)$

The isochores fall into three groups: $\rho \leq 0.91$ g/cm^3, $0.92 \leq \rho \leq 1.04$ g/cm^3 and $\rho \geq 1.05$ g/cm^3.

chores instead of isobars. The graph was first made to verify that the DSE equation fails to hold along isochores as well as isobars. The DSE equation predicts straight lines on such plots, and it is clear that the equation does not hold, with $\tau_\alpha/(T\tau_2)$ becoming less linear as temperature is lowered.

The salient features of Figure 4.1 are two striking gaps that exist over the whole range of temperature, though they are hard to see at the lowest temperatures due to the change in slope and poor statistics. They separate the value of $\tau_\alpha/(T\tau_2)$ into three regions: (i) $\rho < 0.91$ g/cm^3; (ii) $0.92 < \rho < 1.04$ g/cm^3; and (iii) $\rho > 1.05$ g/cm^3. Between the densities 0.91 and 0.92 g/cm^3 and between 1.04 and 1.05 g/cm^3 there is a significant change in behavior. Figure 4.2 plots the difference
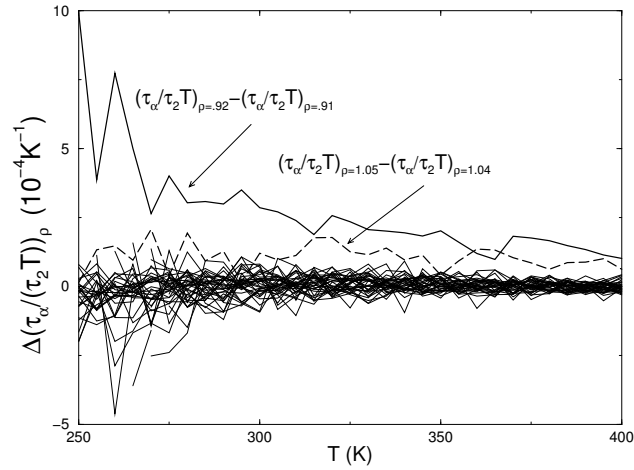
Figure 4.2: Changes in isochores of $\tau_\alpha/(T\tau_2)$

Shown are the differences between neighboring isochores from Figure 4.1. At low temperatures, differences between all isochores are great, but at high temperatures, the differences between the $\rho = 0.91$ and the $\rho = 0.91$ g/cm^3 isochores as well as between the $\rho = 1.05$ and the $\rho = 1.04$ g/cm^3 isochores are significantly greater than differences between all other isochores.

of the value of $\tau_\alpha/(T\tau_2)$ between neighboring isochores, confirming that there are two shifts in $\tau_\alpha/(T\tau_2)$ that are abnormal. Figure 4.3 averages these differences over temperature to make the changes more readily apparent.

Figures 4.5 and 4.6 show the same quantity but plotted along isotherms as a function of density. Figure 4.6 includes two plots, one of which shows τ_α/τ_2 without the T dependence. Both plots shift isotherms vertically for visual clarity. The T dependence does not affect the results significantly. The isothermal paths are like vertical slices going down the isochoric paths of Figure 4.1, and they show the abrupt changes between 0.91 and 0.92 g/cm^3 as well as between 1.04 and 1.05 g/cm^3.

These two abnormalities at 0.91 and 1.04 g/cm^3 are a result of underlying behavior in τ_α, and are more clearly defined in the ratios $\tau_\alpha/(T\tau_2)$ or τ_α/τ_2 because
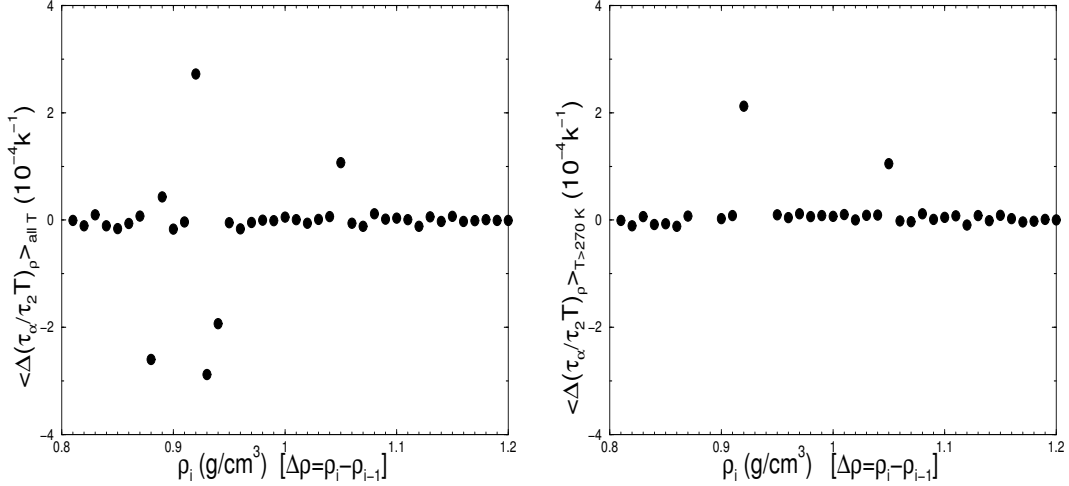
Figure 4.3: Average values of changes in isochores of $\tau_\alpha/(T\tau_2)$

The plots show the average value of the differences in $\tau_\alpha/(T\tau_2)$ between neighboring isochores (see Figure 4.2). The average is calculated over all temperatures (left), and only temperatures above 270 K (right), which reduces the effect of the low temperature noise.

τ_2 acts as a baseline. Viewed by itself, τ_α shows faint abnormalities, while τ_2 does not; see Figure 4.7. This means that the cause of the abrupt change in behavior is mainly a translational property. The change in τ_α appears almost discontinuous at $\rho = 0.91$ g/cm^3 and $\rho = 1.04$ g/cm^3; however, the resolution in the density, as detailed as it is, is not detailed enough to make us believe that the change is discontinuous. In addition, the amplitude of the change is nearly the same as the statistical fluctuations.

To understand the origin of this change, we show the phase behavior of ST2 in the $T - P$ plane (Figure 4.8). The phase diagram shows that the critical point terminating the line of the first-order liquid liquid transition occurs at $\rho \approx$ 0.91 g/cm^3. Hence, a plausible explanation for the sharp viscosity change at 0.91 g/cm^3 is the existence of a "Widom line". A Widom line can be thought of as a continuation of a phase co-existence line past a critical point. In crossing the
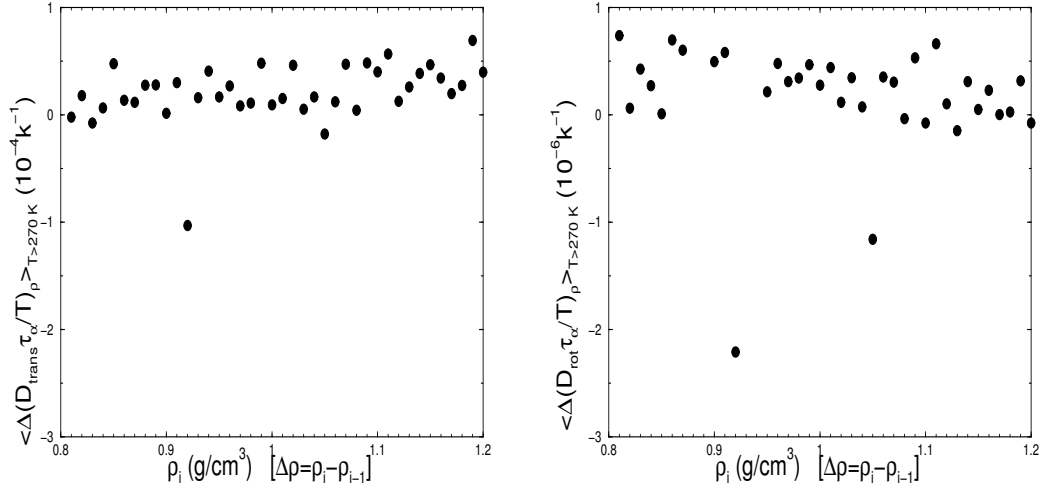
Figure 4.4: Average values of changes in isochores of $\tau_\alpha D/T$
Similar plots to Figure 4.3 but with $\tau_\alpha D_{trans}/T$ (left) and $\tau_\alpha D_{rot}/T$ (right), averaged over all temperatures above 270 K. Plotting the values along isochores is not insightful due to noise, but we can see behavior at 0.91 and 1.05 g/cm^3 by plotting the average differences. The effect is still strongest in $\tau_\alpha/(\tau_2 T)$.

phase transition line there are discontinuous changes in first order quantities (like density); crossing a Widom line is not a first-order phase transition, but there are marked changes in properties over a narrow density range. A Widom line extends from any critical point for the simple reason that response functions (e.g. specific heat and compressibility) must diverage along a path through the critical point; thus along a path near, but not through, the critical point, response functions will show a maximum. Similarly, for first-order quantities like ρ, there will be a sharp but continuous change upon crossing a Widom line.

For example, the gas-liquid co-existence line produces a Widom line. If liquid water is above P_C but below T_C and then decompressed isothermally, it will show a discontinuous change in volume due to crossing the co-existence line and becoming a gas. If the fluid is above both P_C and T_C and decompressed isothermally, there will be a sharp but continuous change in volume and it will still be just a "fluid".
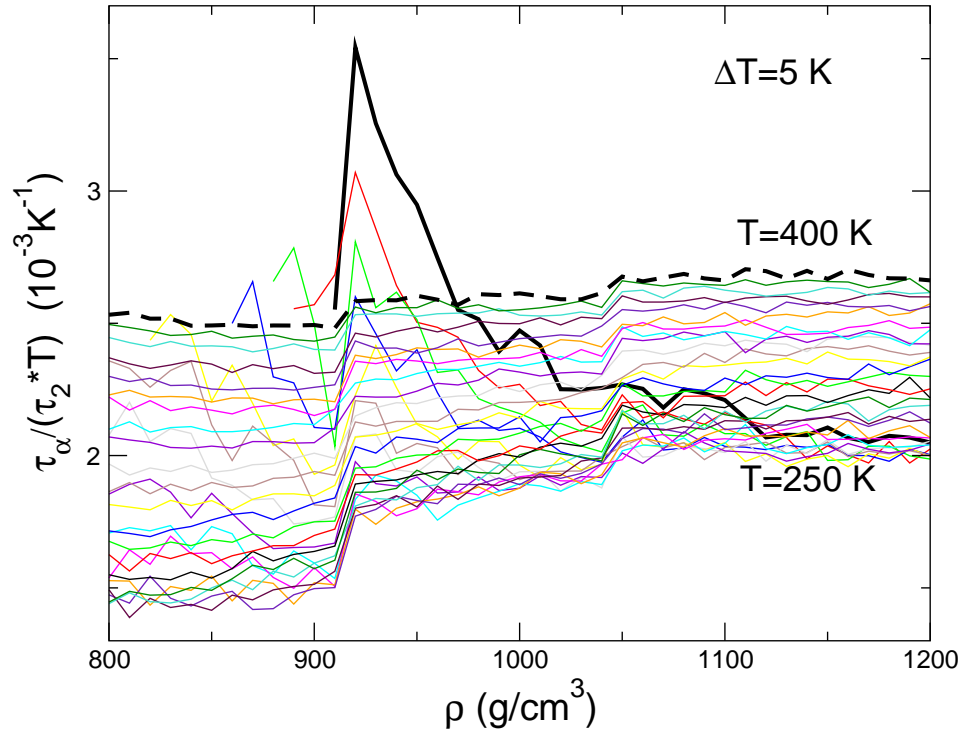
Figure 4.5: Isotherms of $\tau_\alpha/(T\tau_2)$

In practice, it is extremely difficult to distinguish sharp continuous transitions from discontinuous ones.

Crossing a Widom line at statepoints close to a critical point will create much sharper changes in response variables than crossing the Widom line at statepoints farther away. Thus magnitudes of changes across the Widom line decay until it becomes impossible to define the Widom line. In addition, the Widom lines for various properties typically separate as the distance from the critical point increases, meaning that the maximum values of, say, specific heat and compressibility, may not be at the same statepoint (see Fig. 1.7). For ST2 water, the value of the proposed liquid-liquid critical point C' is at $T_{C'} \approx 245 \pm 5$ K, $P_{C'} \approx 180 \pm 10$ MPa and $\rho_{C'} \approx 0.91 \pm .01$ g/cm^3 (Figure 4.8). Using Figure 4.8, it is difficult to

accurately estimate $\rho_{C'}$. Changing to a $T - \rho$ diagram (Figure 4.9) simplifies estimation of the critical density $\rho_{C'} \approx 0.91 \pm .01$ g/cm^3 since it must lie at the apex of the spinodal. Thus, decompressing supercooled water from 220 to 140 MPa isothermally at 160 K would cross the liquid-liquid Widom line making sharp changes in the volume (with specific heat and compressibility taking very large values) and would resemble a first order phase transition. Crossing the Widom line at 350 K (where ST2 is no longer supercooled) would intuitively make relatively smooth changes in the volume, and specific heat and compressibility would not increase much.

While a Widom line is typically defined in terms of thermodynamic properties, it is also possible to define a Widom line in terms of relaxation behavior, since sharp changes in thermodynamics are typically accompanied by sharp changes in dynamics. If we interpret the abrupt changes in τ_α/τ_2 as the crossing of a Widom line – which is a natural idea, since the first change in τ_α occurs close to the critical density – then there are strong implications. Because the sharp change persists to our highest temperature data (400 K, which may be very loosely interpreted as a temperature of $\approx 90°$C in real water), this implies that the Widom line for τ_α has not decayed much over 150 K, which is unexpected and has not been previously observed.

The second abrupt change in τ_α occurs at 1.04 g/cm^3 and is less clearly interpreted since we observe no low T phase transition at this density. Because τ_α/τ_2 at this density exhibits very similar behavior to the change of τ_α/τ_2 at $\rho = 0.91$ g/cm^3, it is natural to suggest that it is another Widom line. Since only one Widom line (for a given property) leaves a critical point, a second Widom line implies the existence of a second liquid-liquid critical point. We note that the second change in τ_α does not require the existence of a second liquid-liquid critical point; it is possible that it just a shift in dynamical behavior, resulting from a sharp (but continuous) thermodynamic change at lower T. However, given the behavior at $\rho = 0.91$ g/cm^3, the existence of a second abnormality at 1.04 g/cm^3 lends circumstantial evidence to the existence of a second liquid-liquid critical point. The existence of a family of liquid states would be analogous to the fact

that there is a family of crystalline states with more than 15 distinct structures (and still more are being discovered). Since the presence of multiple crystalline states is termed polymorphism, the presence of multiple liquid states is sometimes referred to as polyamorphism.
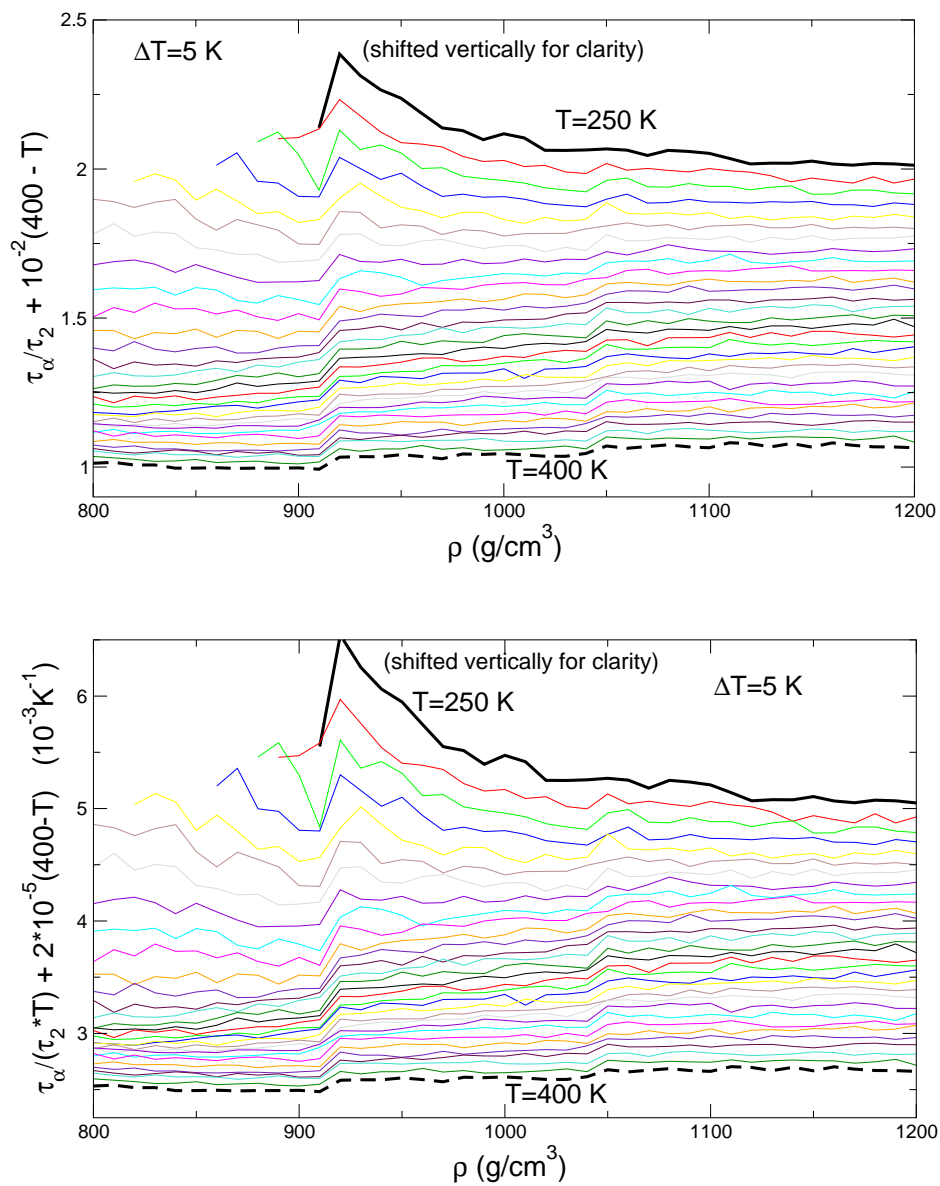
Figure 4.6: Isotherms of $\tau_\alpha/(T\tau_2)$ and $\tau_\alpha/(\tau_2)$, with isotherms shifted vertically for clarity.
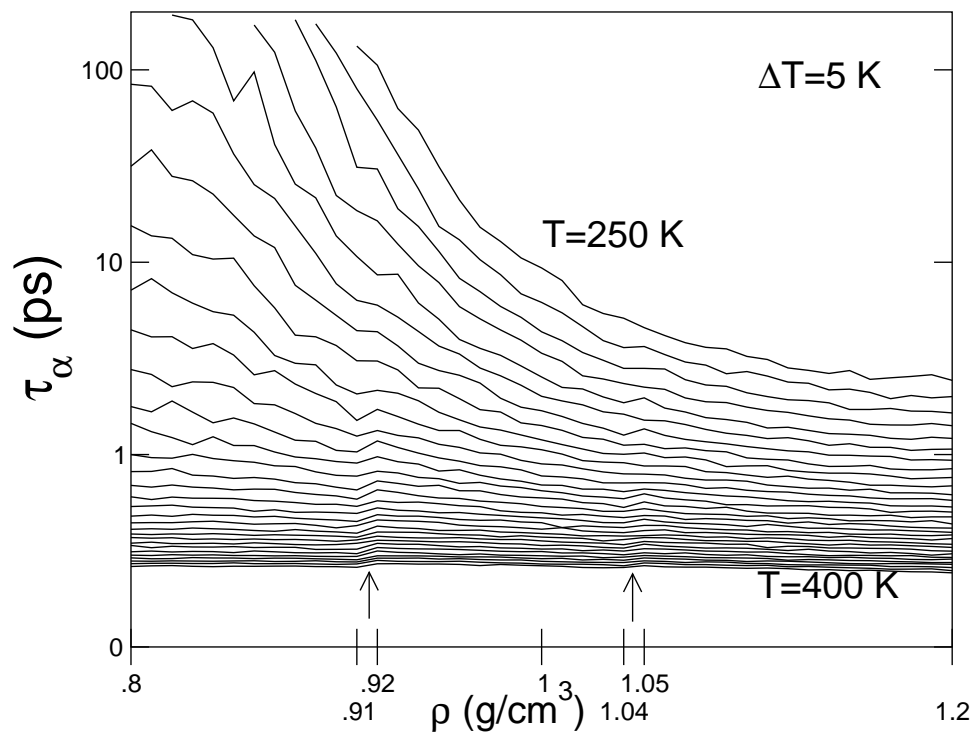
Figure 4.7: Isotherms of τ_α

Enlargement of left plot in Figure 3.9, suggesting that the anomalous behavior in $\tau_\alpha/(T\tau_2)$ is caused by τ_α. τ_2 does not show similar anomalies.

4.1 The Liquid-Liquid Transition

Poole and co-workers [6, 42] first suggested in 1992 that water may have a liquid-liquid transition, with a co-existence line terminating in a second critical point C'. This second critical point theory would explain the different types of glass (HDA and LDA) as the glassy forms of two distinct types of liquids (HDL and LDL). Above the critical point, liquid water would once again only have its one usual form. Experimental work has placed $T_{C'}$ just below the homogeneous nucleation temperature, and therefore it cannot be probed directly by experiments. It should be mentioned that there are also competing theories, notably the stability limit theory proposed by Speedy in 1982 [23] that suggests there is a re-entrant spinodal from the liquid-gas transition, and the singularity-free scenario [24], which invokes no singularities or spinodals, but instead has sharp but continuous changes in thermodynamic properties. Poole et al. [42] provide strong evidence against the stability limit theory, and there has been considerable evidence suggesting the liquid-liquid critical point hypothesis [28, 27, 29].

Figure 4.8 shows the location of C' in the phase diagram of ST2 water. The location of C' in real water is suggested to be at $\approx$ 215 K and $\approx$ 180 MPa (Figure 1.5), which is roughly 30 K and 80 MPa below the critical point in ST2, in agreement with the differences found at the TMD.
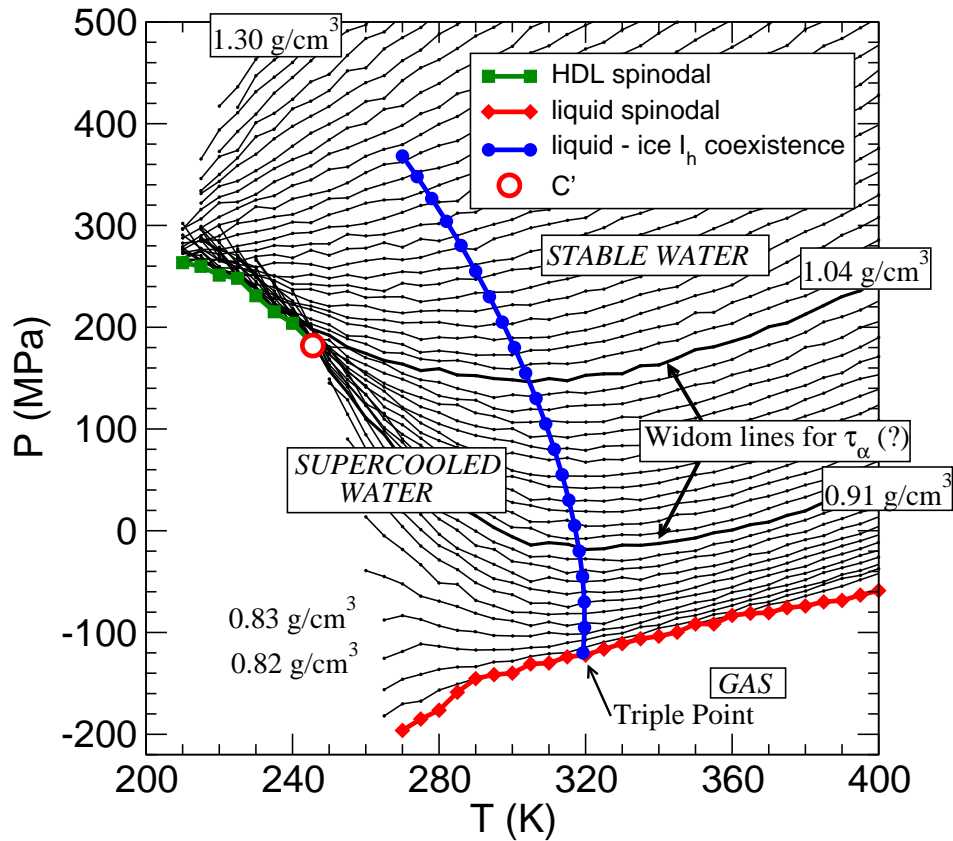
Figure 4.8: Experimentally known $P - T$ phase diagram of ST2 water
The HDL-LDL spinodal is shown, while the HDL-LDL coexistence line and the LDL-HDL spinodal line are not shown. All three lines terminate in the critical point C'. The black lines are isochores. Not shown is the liquid-gas critical point C which is located above 400 K.
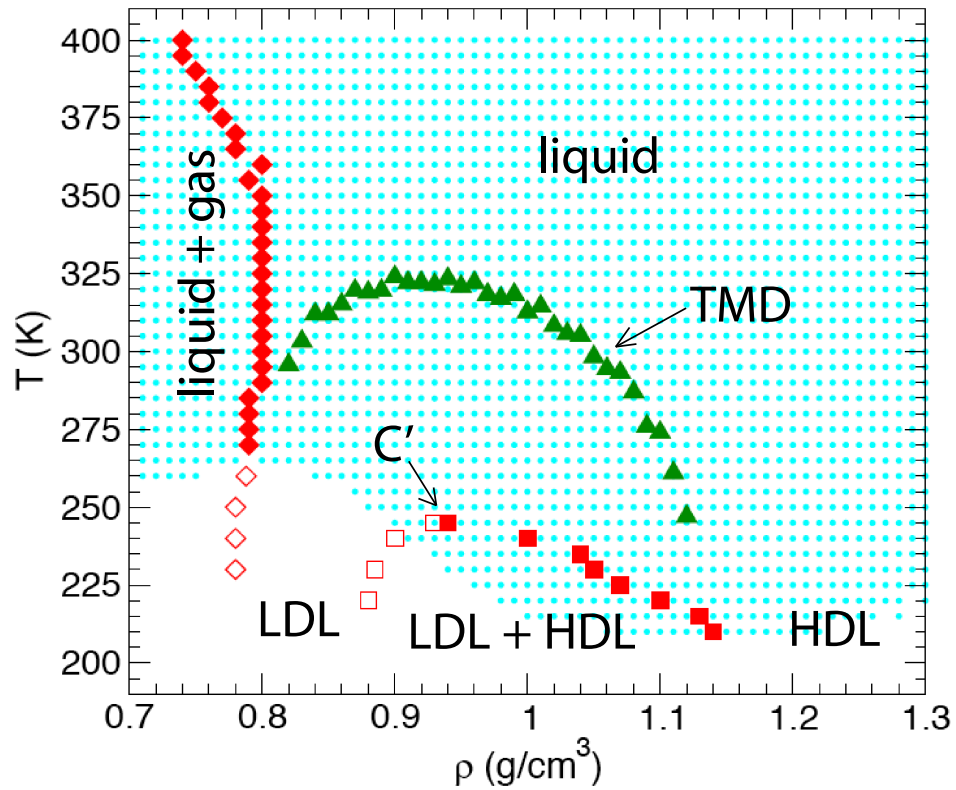
Figure 4.9: Experimentally known $T - \rho$ phase diagram of ST2 water

The HDL-LDL and LDL-HDL spinodals are shown (red squares), as well as the temperature of max density (TMD) in green triangles. The red diamonds show the liquid-gas spinodal. The critical point C' is at $\rho \approx 0.91$ g/cm^3. From P.H. Poole (private communication).

4.2   Multiple Liquid-Liquid Transitions

There has been recent evidence to suggest that water may have more than one liquid-liquid first-order phase transitions. Brovchenko et al. [7] found evidence for three liquid-liquid transitions in Monte Carlo simulations of ST2. However, the method used tends to promote phase separation when the length scale of density fluctuations grows, and hence may spuriously indicate a phase transition where there is none; their findings have not yet been tested against traditional methods where such effects do not exist. They suggest that the four liquid phases in their simulations correspond to LDA, hyperquenched amorphous water, HDA, and VHDA. Many researchers believe LDA and hyperquenced amorphous water to be the same phase, and more recent evidence has suggested that HDA and VHDA are no separate phases either [14]. The density of the second liquid-liquid transition found by ref. [7] is ≈ 1.05 g/cm^3, very close to the density of the second Widom line that we observe. These complementary evidence provide stronger reasons to consider the possibility of multiple liquid-liquid critical points.

Most recently [64], Brovchenko et al. simulated additional models of water. In TIP4P, TIP5P and SPCE/E models they found two liquid-liquid transitions, as well as the previously reported three transitions in ST2. They also note that the locations of these transitions are highly sensitive to the water model and its implementation.

Computer simulation of a soft-core potential of several discontinuous steps [65] and of a square-well potential with a repulsive shoulder [66] have shown clear evidence of multiple liquid-liquid transitions, though these potentials are not related to water. General theories which allow liquid-liquid transitions and which suggest critical points at negative pressures [15] have been put forward but have not been widely accepted. There has also been some experimental evidence for multiple liquid-liquid transitions [67] using difference and double-difference near-infrared spectroscopy with a new band deconvolution technique.

Chapter 5

Conclusion

As temperature decreases, the temperature dependence of many quantities changes in a fundamental way. Table 5.1 reviews the behavior at high temperatures and low temperatures.

High T	Low T	Crossover T
Ballistic-to-diffusive	Caging effects	not calculated
Arrhenius behavior	non-Arrhenius Behavior	T_A
SE equation holds	SE equation doesn't hold	T_{SE}
DSE equation holds	DSE equation doesn't hold	not calculated
D_{trans} and D_{rot} proportional	D_{trans} and D_{rot} not proportional	T_α
D_{trans} and τ_2^{-1} proportional	D_{trans} and τ_2^{-1} not proportional	T_β
D_{rot} and τ_2^{-1} proportional	D_{rot} and τ_2^{-1} not proportional	not calculated
Spatial homogeneity	Spatial heterogeneity	not calculated

Table 5.1: Summary of behavior at high and low temperatures

While we found rough estimates of some of the crossover temperatures from table 5.1 (Figure 5.1), this was not the end-goal of the research. More important were the qualitative results, namely that the Debye-Stokes-Einstein equation does not hold at low temperatures, disagreeing with previous literature with the exceptions of refs. [60, 50, 59, 61]. Previous literature have used the assumption $D_{rot} \propto 1/\tau_2$. Because we have data on both D_{rot} and τ_2, we tested this assumption and found it to fail at low temperatures. The DSE equation failed to hold at low
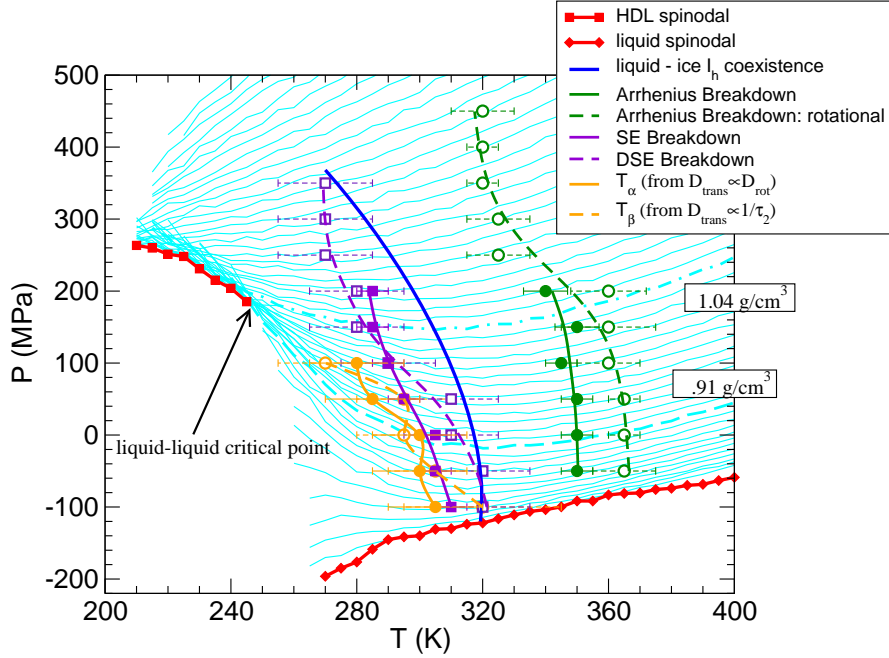
Figure 5.1: Summary of crossover temperatures

temperatures regardless of whether we used D_{rot} or $1/\tau_2$. This result may have implications on theories of dynamic heterogeneities. We also confirmed that the Stokes-Einstein equation does not hold, expected from past work.

Another major result of this work is that we find that *rotational* diffusion is enhanced when compared to translational diffusion at sufficiently low temperatures. This is at odds with claims from much of the previous literature for simple glass formers [48, 49, 54, 40, 56], but is consistent with the simulations of [61], other experiments on glass formers [59, 60, 50] and the experimental results of [62] for water. More extensive studies of simple glass forming models would be valuable to determine if the apparent conflict with some experiments is a result specific to water or systematic across models.

The most unexpected result was that at all temperatures studied, there is an apparent precursor in τ_α to liquid-liquid phase transitions at lower temperatures along the critical isochore $\rho = 0.91$ g/cm³. We do not expect this to be a remnant

of the simulation protocol (in which high temperature configurations were used to seed lower temperature configurations) because the isochore lines were simulated completely independently from each other. Moreover, the data show that the jumps in τ_α were statistically significant. A useful extension of this work would be to simulate many independent runs along isochores near the critical densities of 0.91 g/cm^3 and 1.04 g/cm^3, perhaps with finer resolution in the density, such as 0.002 g/cm^3 spacing between 0.91 and 0.92 g/cm^3.

At $\rho = 1.04$ g/cm^3, the τ_α shows a similar signature to that found along the critical isochore. Since the lower density irregularity is a remnant of the LDL-HDL co-existence line, it is plausible that the higher density irregularity is the remnant of some other liquid-liquid co-existence line. However, we point out that there is no dynamic or thermodynamic theory that requires that the 1.04 g/cm^3 irregularity intersects a critical point. However, our results do add to the plausibility of such transitions, and may influence future reseach into the possibility of such transitions.

There are many unresolved questions about supercooled water. What are the relations between the different crossover temperatures defined in Table 5.1? What are the mechanisms that cause the transitions? Is there definitely a liquid-liquid transition, and is there more than one liquid-liquid transitions? How are the thermodynamics and dynamics related? We offer the results from this thesis in the hope that our work will help answer these questions.

Bibliography

[1] P. G. Debenedetti, *Metastable Liquids* (Princeton Univ. Press, Princeton, 1996).

[2] C. A. Angell, Science **267**, 1924 (1995).

[3] P. G. Debenedetti and H. E. Stanley, Physics Today **56**, 40 (2003).

[4] P. G. Debenedetti and F. H. Stillinger, Nature **410**, 259 (2001).

[5] C. Zandonella, New Scientist **186**, 35 (2005).

[6] P. H. Poole, F. Sciortino, U. Essmann, and H. E. Stanley, Nature **360**, 324 (1992).

[7] I. Brovchenko, A. Geiger, and A. Oleinikova, J. Chem. Phys. **118**, 9473 (2003).

[8] F. P. Bundy, J. Chem. Phys. **38**, 618 (1963).

[9] N. S. Fateeva and L. F. Vereshchagin, Pis'Ma Zh. Eksp. Teor. Fiz. **13**, 168 (1971).

[10] M. van Theil and F. H. Ree, Phys. Rev. B **49**, 3591 (1993).

[11] J. N. Glosli and F. H. Ree, Phys. Rev. Lett. **82**, 4659 (1999).

[12] M. Togaya, Phys. Rev. Lett. **79**, 2474 (1997).

[13] M. P. Grumbach and R. M. Martin, Phys. Rev. B **54**, 15730 (1996).

[14] H. E. Stanley *et al.*, Phil. Trans. R. Soc. **363**, 509 (2005).

[15] H. Tanaka, Phys. Rev. E **62**, 6968 (2000).

[16] P. G. Debenedetti, J. Phys.: Condens. Matter **15**, 1669 (2003).

[17] H. E. Stanley *et al.*, Phys. Chem. Chem. Phys. **2**, 1551 (2000).

[18] G. P. Johari, A. Hallbrucker, and E. Mayer, Nature **330**, 552 (1987).

[19] A. Hallbrucker, E. Mayer, and G. P. Johari, J. Phys. Chem. **93**, 4986 (1989).

[20] C. A. Angell, Chem. Rev. **102**, 2627 (2002).

[21] V. V. S. Borick and C. A. Angell, Science **294**, 2335 (2001).

[22] O. Mishima, L. D. Calvert, and E. Whalley, Nature **310**, 393 (1984).

[23] R. J. Speedy, J. Phys. Chem. **86**, 982 (1982).

[24] S. Sastry, F. Sciortino, P. G. Debenedetti, and H. E. Stanley, Phys. Rev. E **53**, 6144 (1996).

[25] P. G. Debenedetti, Nature **392**, 127 (1998).

[26] L. P. N. Rebelo, P. G. Debenedetti, and S. Sastry, J. Chem. Phys. **109**, 626 (1998).

[27] O. Mishima, Phys. Rev. Lett. **85**, 334 (2000).

[28] O. Mishima and H. E. Stanley, Nature **392**, 164 (1998).

[29] O. Mishima and Y. Suzuki, J. Chem. Phys. **115**, 4199 (2001).

[30] L. D. Landau and E. M. Lifshitz, *Statistical Physics* (Pergamon Press, London, 1980).

[31] D. Chandler, *Introduction to Modern Statistical Mechanics* (Oxford University Press, Oxford, 1987).

[32] F. W. Starr, Ph.D. thesis, Boston University, 1999.

[33] C. A. Angell, in *Water: A Comprehensive Treatise*, edited by F. Franks (Plenum, New York, 1982).

[34] P. G. Debenedetti and H. E. Stanley, Phys. Today **56**, 40 (2003).

[35] J. P. Hansen and I. R. McDonald, *Theory of Simple Liquids* (Academic Press, London, 1986).

[36] L. D. Landau and E. M. Lifshitz, *Hydrodynamics* (Pergamon Press, Oxford, 1959).

[37] M. P. Allen and D. J. Tildesley, *Computer Simulation of Liquids* (Oxford Univ. Press, Oxford, 1987).

[38] M. D. Ediger, Annu. Rev. Phys. Chem. **51**, 99 (2000).

[39] H. Sillescu, J. Non-Cryst. Sol. **243**, 81 (1999).

[40] M. T. Cicerone and M. D. Ediger, J. Chem. Phys **104**, 7210 (1996).

[41] F. H. Stillinger and A. Rahman, J. Chem. Phys. **60**, 1545 (1974).

[42] P. H. Poole, F. Sciortino, U. Essmann, and H. E. Stanley, Phys. Rev. E **48**, 3799 (1993).

[43] H. J. C. Berendsen, J. R. Grigera, and T. P. Stroatsma, J. Phys. Chem. **91**, 6269 (1987).

[44] W. L. Jorgensen *et al.*, J. Chem. Phys. **79**, 926 (1983).

[45] M. W. Mahoney and W. L. Jorgensen, J. Chem. Phys. **114**, 363 (20001).

[46] J.-P. Ryckaert, G. Ciccotti, and H. J. C. Berendsen, J. Comput. Phys. **23**, 327 (1977).

[47] O. Steinhauser, Mol. Phys. **45**, 335 (1982).

[48] F. Fujara, B. Geil, H. Sillescu, and G. Fleischer, Z. Phys. B. **88**, 195 (1992).

[49] F. R. Blackburn *et al.*, J. Non-Cryst. Solids **172**, 256 (1994).

[50] E. Rössler, Phys. Rev. Let. **65**, 1595 (1990).

[51] P. D. Hyde, T. E. Evert, and M. D. Ediger, J. Phys. Chem. **93**, 2247 (1990).

[52] T. Dries *et al.*, J. Chem. Phys. **88**, 2139 (1988).

[53] F. H. Stillinger and J. A. Hodgdon, Phys. Rev. E **50**, 2064 (1994).

[54] M. T. Cicerone and M. D. Ediger, J. Phys. Chem. **97**, 10489 (1993).

[55] G. Heuberger and H. Sillescu, J. Phys. Chem. **100**, 15255 (1996).

[56] F. R. Blackburn, C.-Y. Wang, and M. D. Ediger, J. Phys. Chem. **100**, 18249 (1996).

[57] P. Bordat, F. Affouard, M. Descamps, and F. Müller-Plathe, J. Phys.: Condens. Matter **15**, 5397 (2003).

[58] Y. Jung, J. Garrahan, and D. Chandler, Phys. Rev. E **69**, 061205 (2004).

[59] L. Andreozzi, A. D. Schino, M. Giordano, and D. Leporini, Europhys. Lett. **38**, 449 (1997).

[60] L. Andreozzi, A. D. Schino, M. Giordano, and D. Leporini, J. Phys. Condens. Matter **8**, 9605 (1996).

[61] C. D. Michele and D. Leporini, Phys. Rev. E **63**, 036702 (2001).

[62] E. Lang and H.-D. Lüdemann, J. Chem. Phys. **67**, 718 (1977).

[63] E. Lang, H.-D. Lüdemann, L. Piculell, and D. Müller, J. Chem. Phys **93**, 4796 (1990).

[64] I. Brovchenko, A. Geiger, and A. Oleinikova, arXiv.org:cond-mat/0503584, March 2005 (unpublished).

[65] S. V. Buldyrev and H. E. Stanley, Physica A **330**, 124 (2003).

[66] J. A. White, Physica A **346**, 347 (2005).

[67] D. E. Khoshtarija *et al.*, ChemPhysChem **5**, 1398 (2004).